TECHNISCHE
UNIVERSITÄT
WIEN

VIENNA
UNIVERSITY OF
TECHNOLOGY

DIPLOMARBEIT

Phase behaviour of the Penetrable Sphere Model

Ausgeführt am Institut für
Theoretische Physik
der Technischen Universität Wien
unter der Anleitung von
Ao. Univ. Prof. Dr. Gerhard Kahl

durch
Georg Falkinger
Ödwiesenstrasse 3, 4040 Linz

18. 10. 2007

Contents

1 Introduction

Generally speaking, liquids can be divided in two groups. So called *simple or atomic liquids* (such as noble gases) which are either one component systems or mixed, consisting of more species of particles. Such liquids are characterized by a two-body interaction potential which is dominated by electrostatic forces, on the one hand, and the Pauli exclusion principle on the other hand. Obviously, due to the latter any interaction potential of a simple liquid diverges at short distances. Typical theoretical models for such simple liquids are the Lennard-Jones or the hard core Yukawa potential.

Liquids like milk, where in a simplified view, proteins are dispersed in water do not refer to this first group. Such liquids form a special class of soft matter dubbed *colloidal or complex liquids*, which consist of relativly large, mesoscopic particles, dispersed in a solvent of comparatively small particles, where the term mesoscopic characterizes the size of the particles, which ranges from 1nm to 1μm. Other examples for liquids of this group are ink, paint, detergents and gels. Hence, the class of colloidal liquids comprises a wide variety of substances, that we encounter in our every day lives, and that are relevant in numerous industrial applications. Moreover, all bodily fluids are colloidal liquids, indicating the importance of this class of liquids for medicine and biology.

Due to the large size of the mesoscopic particles, which themselves consist of up to several hundreds of atoms, and due to the presence of the solvent particles, the number of degrees of freedom in colloidal systems is extremly high compared to simple liquids. This complexity is undoubtedly an important factor that causes the broad diversity of observed phenomena and the exotic macroscopic behaviour of such liquids.

In order to simplify the problem, *effective interactions* are introduced on the basis of the following considerations. The solvent can be viewed as a homogeneous liquid, which is not affected by the movement of the mesoscopic particles. Furthermore, the degrees of freedom of the constituent microscopic particles are integrated out by suitable coarse-graining methods, replacing thus the mesoscopic particle by a structurless homogeneous particle [1]. This averaging procedure is realized while fully conserving the thermodynamic properties. Thus, one can derive an effective interaction, which depends only on a few paremeters such as the centers of mass of the mesoscopic particles. This effective interaction or effective potential is equivalent to the two-particle interaction potential for simple liquids. Therefore the same the-

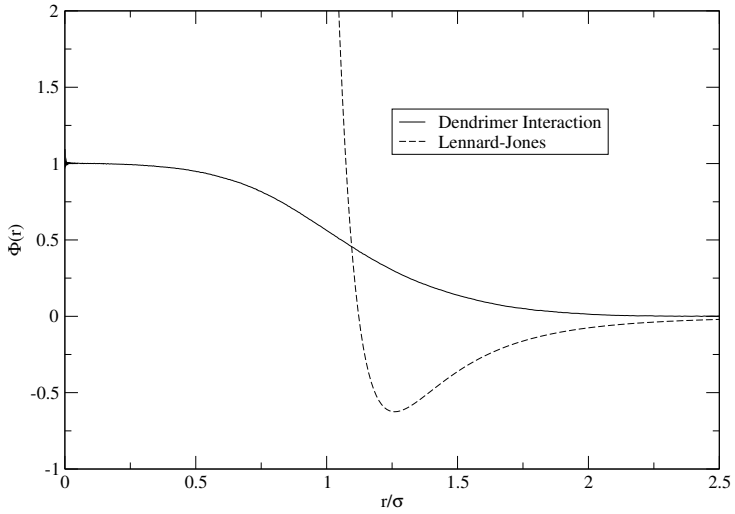

Figure 1: Comparison of the Lennard-Jones potential and an effective potential derived for dendrimers via computer simulations [2].

oretical methods, that are used for simple liquids can be applied to colloidal liquids.

Not only the theoretical but also the experimental access to colloidal systems is eased, since the effective interaction can be measured, for instance by means of atomic force microscopy (AFM) or by means of optical tweezers. A different approach is to perform computer simulations on model systems. Hence, the concept of effective interactions allows a close interdisciplinary contact between theory and experiment.

One striking feature which distinguishes effective potentials of complex fluids from typical potentials of atomic systems like the Lennard-Jones or hard core Yukawa potential, is the fact, that they do not necessarily diverge at the origin. Such so-called *bounded potentials* remain finite, as the distance between two particles vanishes, and thus the particles are allowed to fully overlap while avoiding overlap of the microscopic constituents. This is for example the case in a system of polymer chains [1], where the whole chain is modelled as one effective particle, and the effective potential depends only on the distance of the centers of mass of the particles. Figure 1 depicts a typical bounded potential, derived for dendrimers via computer simulations [2] in comparison with a Lennard-Jones interaction.

The boundedness of the potential gives rise to a rather exotic phase be-

haviour, unheard-of in the context of simple liquids. Among those are the *re-entrant melting* and the *clustering* behaviour. In the first case a system freezes at a given temperature if the density is increased, only to re-melt upon further compression. In the second case aggregates of overlapping particles emerge and arrange, if the density is increased at a given temperature, in an ordered lattice; the aggregates are referred to as clusters.

The aim of this thesis is to predict the phase behaviour of a liquid, which is characterized by a specific bounded model interaction namely the Penetrable Sphere Model (PSM). The rest of this thesis is organized as follows. In chapter 2 we will present the PSM and the closely related core modified Penetrable Sphere Model (cmPSM). In chapter 3 we review the different methods that were used in this work, i.e., Integral Equation Theory (IET), Density Functional Theory (DFT) and Monte-Carlo Simulations. In the results section, chapter 4, we start by comparing the simulation results to the results obtained from IET and DFT, respectively. Moreover we present the phase diagrams of the investigated models and discuss the results for the structure of the solid phase as obtained by DFT. Apart from that, we will compare our numerical data to theoretical predictions proposed in recent publications. In chapter 5 we summarize our results and draw conclusions that seem relevant to us.

2 The models

2.1 The Penetrable Sphere Model (PSM)

The system, that is investigated in this work, consists of N identical and spherically symmetrical particles, which are confined in a volume V. The Penetrable Sphere Model (PSM), which is a specific form of a bounded two-body interaction potential, reads as:

$$\Phi_{\mathrm{PSM}}(r) = \begin{cases} \epsilon, & r \leq \sigma \\ 0, & r > \sigma \end{cases} . \tag{1}$$

ϵ is an energy parameter and σ is the diameter of the particle. If two particles are seperated by a distance $r > \sigma$, they do not interact. At smaller seperations, however, the particles overlap and a constant cost of energy has to be paid. Due to the discontinuity at σ this interaction potential seems unphysical at first glance and one might consider it of purely academic interest. The justification of the PSM lies in the fact, that it features all characteristic properties of bounded potentials, while having a relatively simple form. The PSM can be seen as a limiting case of the Generalized Gaussian Core Model (GEM) which is defined as

$$\Phi_{\mathrm{GGCM}} = \epsilon \exp[-(r/\sigma)^n]. \tag{2}$$

For $n = 2$ the GEM leads to the Gaussian Core Model (GCM), introduced by Stilinger *et al.* [3] whereas in the limit $n \to \infty$ the PSM is recovered as shown in figure 2. At temperature $T = 0$ the PSM clearly reduces to the Hard Sphere Model.

Up to now the PSM has been investigated with a wide variety of theoretical tools, e.g., [4][5][6][7][8][9].

Some important integrals can be solved analytically and the sharp cut-off in the potential obsoletes background corrections in MC simulations. In contrast to GGCM models, the particle radius is well defined and so are the clusters in the solid phase. This helps to save computer time.

Apart from theoretical justifications for the PSM, there is also a more practical reason put forward by Marquest and Witten [10], who explained the experimentally observed crystallization of copolymer mesophases on the ba-

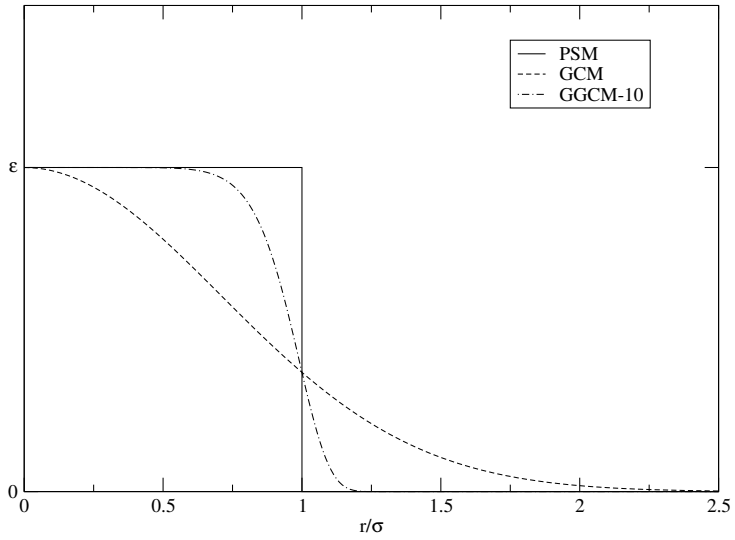

Figure 2: The Penetrable Sphere Model (PSM) compared to the Gaussian Core Model (GCM) and the Generalized Gaussian Core Model with index 10 (GEM-10).

sis of the PSM.

2.2 The core modified Penetrable Sphere Model (cmPSM)

The Core Modified Penetrable Sphere Model (cmPSM) is closely related to the PSM. With respect to the ordinary PSM it has a core region with a relative attraction, the form of which is tuned by two dimensionless parameters τ and κ. The interaction of the cmPSM reads as:

$$\Phi_{\mathrm{cmPSM}}(r) = \begin{cases} \tau\epsilon, & r \leq \kappa\sigma \\ \epsilon, & \kappa\sigma < r \leq \sigma \\ 0, & r > \sigma \end{cases} . \tag{3}$$

The depth of the attractive core is fixed by τ and the range of the attractive core is determined by κ. This model has not yet been dealt with in literature. It was inspired by an effective dendrimer interaction potential extracted from computer simulation. Figure 3 depicts $\Phi_{cmPSM}(r)$ with parameters $\kappa = 0.3$ and $\tau = 0.7$ as well as a typical dendrimer interaction as predicted by Mladek *et al.* [2].

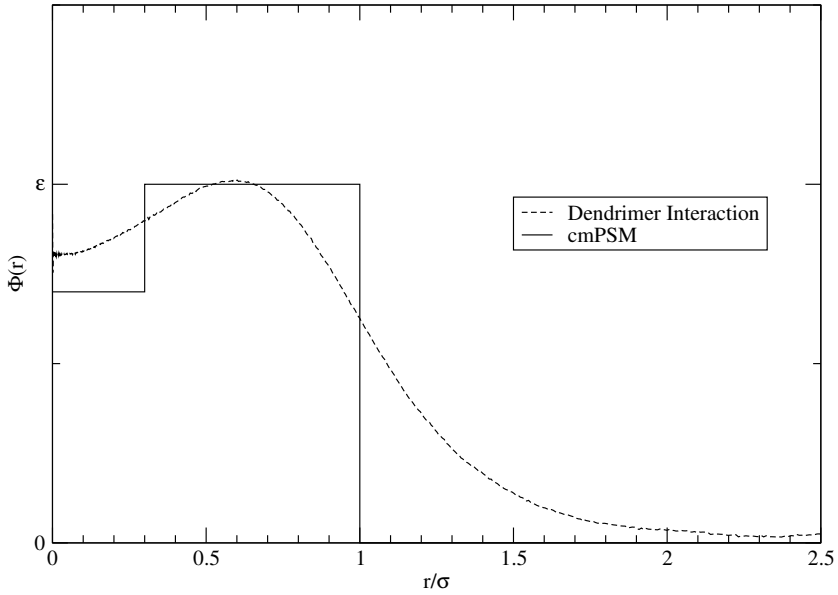

Figure 3: The core modified Penetrable Sphere Model (cmPSM) with parameters $\kappa = 0.3$ and $\tau = 0.7$ compared to a dendrimer interaction as obtained from computer simulation by Mladek *et al.*[2].

2.3 Reduced Units

For the sake of simplicity we introduce the following dimensionless reduced units: The reduced number density is defined as

$$\rho^* \equiv \rho\sigma^3 = \frac{N}{V}\sigma^3. \tag{4}$$

The reduced temperature is defined as

$$T^* \equiv \frac{k_B T}{\epsilon} = \frac{1}{\beta\epsilon}. \tag{5}$$

ϵ is the energy scale, set by the height of the potential, and k_B is the well known Boltzmann constant.

3 Theory

The purpose of this chapter is not only to explain the methods used in this work but also to put them in a broader context of statistical mechanics and liquid state theory.

The section 3.1 on statistical mechanics has its focus on the canonical ensemble and only recalls some fundamental ideas and formulas. A comprehensive introduction to the subject can be found e.g. in reference [11].

The first part of the section 3.2 on Integral Equation and the section 3.4 on Monte-Carlo simulations alike are a compact sum-up of key concepts, a detailed study is provided e.g. by references [12] and [13].

The second part of the section 3.2 on Integral Equation Theory and the section 3.3 on Density Functional Theory contain more exotic formalisms, specifically and rather recently developed for soft systems. These are not subjects of textbooks and therefore receive more attention in this chapter. References will be given in the respective sections. For a theoretical and mathematical background of Density Functional Theory see reference [14].

The last section 3.5 of this chapter presents two important concepts of fluid-solid transitions, which are used in order to determine the phase boundaries.

3.1 Statistical mechanics

The system of interest here consists of N classical, identical particles in a fixed Volume V. The number of particles is fixed, and the temperature T is held at a constant value. This can be achieved by connecting the system to a heat bath or energy reservoir. A thermodynamic state is described by macroscopic parameters such as pressure or temperature. The relation between these parameters is given by equations of state, the ideal gas law being the most prominent example: $PV = Nk_BT \equiv N\beta^{-1}$.

On a microscopic level, the state of the system is given by the postitions and the momenta of the particles. These are the only degrees of freedom if spherically symmetrical particles are considered. In other words, the microscopic state of the system is a point in the $6N$ dimensional phase space.

The dynamics of the system or the trajectory of the said point in phase space are guided by the Hamilton function $H(\mathbf{r}^N, \mathbf{p}^N) = H_{\text{kin}}(\mathbf{p}^N) + V(\mathbf{r}^N)$, where the kinetic term depends only on the momenta $\mathbf{p}^N = \{\mathbf{p}_1, ..., \mathbf{p}_N\}$ of the

particles while the potential depends only on their positions $\mathbf{r}^N = \{\mathbf{r}_1, ..., \mathbf{r}_N\}$, respectively.

Ensemble averages

The connection between microscopic state and macroscopic parameters is established in terms of ensemble averages. An ensemble is a set of microscopic states, all of which correspond to the same macroscopic state. A macroscopic observable A can then be obtained by averaging over all possible microscopic states of the ensemble, the so called ensemble average:

$$\langle A \rangle = \int \int d\mathbf{r}^N d\mathbf{p}^N f(\mathbf{r}^N, \mathbf{p}^N) A(\mathbf{r}^N, \mathbf{p}^N). \tag{6}$$

The probability of finding the system in a particular microscopic state is distributed according to a probability density function $f(\mathbf{r}^N, \mathbf{p}^N)$. Its specific form depends on the macroscopic parameters, which define the thermodynamic state of the system. In the case of a system in contact with a heat bath with fixed N, V and T, the ensemble is called canonical and the probability density function reads as [11]

$$f(\mathbf{r}^N, \mathbf{p}^N) = \frac{1}{N! \hbar^{3N}} \frac{e^{-\beta H(\mathbf{r}^N, \mathbf{p}^N)}}{Q(N, V, T)}, \tag{7}$$

where

$$Q(N, V, T) = \frac{1}{N! \hbar^{3N}} \int \int d\mathbf{r}^N d\mathbf{p}^N e^{-\beta H(\mathbf{r}^N, \mathbf{p}^N)} \tag{8}$$

is the canonical partition function. The Planck constant $\hbar$ establishes the correct connection to quantum mechanics. The prefactor $\frac{1}{N!}$ reflects the fact, that the particles are not distinguishable from one another. Furthermore the system is supposed to be in equilibrium, and the probability density as well as the obsevables do not vary with time.

Helmholtz free energy

The partition function is related to the corresponding thermodynamic potential. In the case of a canonical ensemble, the appropriate thermodynamic

potential is the Helmholtz free energy, given by

$$\beta F(N,V,T) = -\ln Q(N,V,T). \tag{9}$$

Once the thermodynamic potential is known, all thermodynamic properties can be derived in a straightforward way. The internal energy U is given by

$$U = \left[\frac{\partial(\beta F)}{\partial \beta}\right]_{N,V}, \tag{10}$$

and the pressure P is given by

$$P = -\left(\frac{\partial F}{\partial V}\right)_{N,T}. \tag{11}$$

An exact result for the partition function and thus for the exact equations of state are only known for a few simple systems like the ideal gas. For more complex systems, the Helmholtz free energy has to be calculated via approximate approaches.

Since the Hamilton function can be seperated in the kinetic part, which depends only on the momenta and a configurational part that depends only on the positions of the particles, the canonical partition function (8) can be rewritten to give

$$Q(N,V,T) = \frac{1}{N!\Lambda^{3N}} \int d\mathbf{r}^N e^{-\beta V(\mathbf{r}^N)} \equiv \frac{1}{N!\Lambda^{3N}} Z(N,V,T), \tag{12}$$

where $\Lambda = \sqrt{2\pi\beta\hbar^2/m}$ is the thermal de Broglie wavelength and $Z(N,V,T) = \int d\mathbf{r}^N \mathrm{e}^{-\beta V(\mathbf{r}^N)}$ is the configurational part of the partition function. For an ideal gas $Z(N,V,T) = V^N$. Hence also the Helmholtz free energy can be split up, $F = F_{\mathrm{id}} + F_{\mathrm{ex}}$, the first term containing the ideal gas contribution and the second one containing the excess Helmholtz free energy:

$$\beta F_{\mathrm{id}} = \ln \rho + 3 \ln \Lambda - 1 \tag{13}$$

and

$$\beta F_{\rm ex} = -\ln\left(\frac{Z(N,V,T)}{V^N}\right). \tag{14}$$

3.2 Integral Equation Theory

The structure of a homogeneous and isotropic liquid system with N particles and volume V is, most convieniently, described by the pair correlation function $g(|\mathbf{r}-\mathbf{r}'|)$,

$$g(|\mathbf{r}-\mathbf{r}'|) = \frac{1}{\rho^2}\rho^{(2)}(|\mathbf{r}-\mathbf{r}'|) \tag{15}$$

with the homogeneous average density $\rho = \frac{N}{V}$ and the two-particle density correlation function

$$\begin{aligned}\rho^{(2)}(|\mathbf{r}-\mathbf{r}'|) &= \langle\sum_{i=1}^{N}\sum_{j=1}^{N}\delta(|\mathbf{r}-\mathbf{R_i}|)\delta(|\mathbf{r}'-\mathbf{R_j}|) - \\ &- \sum_{i=1}^{N}\delta(|\mathbf{r}-\mathbf{R_i}|)\delta(|\mathbf{r}'-\mathbf{R_i}|)\rangle_N. \end{aligned}\tag{16}$$

The $\mathbf{R}_i$ are position vectors of the particles in a given configuration and the brackets $\langle\ldots\rangle_N$ denote an ensemble average. Physically, the pair correlation function is a measure for the probability of finding two particles at a distance $r = |\mathbf{r}-\mathbf{r}'|$ from each other. Since in an ideal gas the particles are fomally completly uncorrelated and $g(r) = 1$, it can also be interpreted as the deviation of a liquid structure from the ideal gas structure. In a crystal the particles are highly correlated due to the ordered lattice and $g(r)$ has sharp peaks at well defined positions, corresponding to the distances of the particles in the lattice. In any case, $\lim_{r\to\infty} g(r) = 1$, which reflects the fact, that at large distances the correlation between two particles vanishes. For practical reasons, the total correlation function $h(r)$ is introduced, which is related to $g(r)$ via $h(r) = g(r) - 1$.

Evaluating equation (16) is equivalent to calculating the exact partition function, which can only be done for simple systems like the ideal gas.

The Ornstein-Zernicke [15] equation gives an heuristic approach instead, defining the total correlation function in terms of a direct correlation function $c(r)$ as

$$h(r) = c(r) + \rho\int d\mathbf{r}'c(|\mathbf{r}-\mathbf{r}'|)h(r'). \tag{17}$$

A formal iterative solution of this equation leads to

$$\begin{aligned} h(r) &= c(r) + \rho \int d\mathbf{r}' c(|\mathbf{r} - \mathbf{r}'|) c(r') + \\ &+ \rho^2 \int \int d\mathbf{r}' d\mathbf{r}'' c(|\mathbf{r} - \mathbf{r}'|) c(|\mathbf{r}' - \mathbf{r}''|) \ldots . \end{aligned} \tag{18}$$

This expression clarifies the physical idea behind the OZ equation. The total correlation between two particles seperated by a distance r is the sum of their direct correlation and all 'indirect' correlations mediated by an increasing number of other particles at distances r', r'', etc. The approach is heuristic because we do not yet know anything about the direct correlation incorporated in the function $c(r)$.

Obviously the OZ equation (17) can not be solved without an additional condition, since it relates two unknown functions. From statistical mechanics one can derive the following exact expression:

$$g(r) = \exp[-\beta\Phi(r) + g(r) - 1 - c(r) + B(r)], \tag{19}$$

where $\Phi(r)$ is the two-body potential and $B(r)$ stands for the so-called bridge function. Equation (19) incorporates the second condition, needed to solve the Ornstein-Zernicke equation. The 'bridge' function has to be approximated, since deriving an exact expression for it is equvalent to finding the exact solution of the partition function of a system, which is only possible for simple systems like the ideal gas.

In literature there exists a large number of approximation schemes ('closures') for $B(r)$, such as the 'Percus-Yevick' (PY) [16], the 'hypernetted-chain' (HNC) [17] or the 'mean spherical approximation' (MSA) [18]. The open question which closure provides the best results for a given system cannot be answered *a priori*. The quality of the results depends strongly on the features of the investigated system.

The OZ equation together with the closure constitute a system of two coupled integral equations which can be solved numerically, delivering the correlation functions $g(r)$, $c(r)$ and $h(r)$ for given density and temperature. This procedure is known as Integral Equation Theory (IET).

None of the correlation functions can be measured directly in **r**-space. The static structure factor $S(Q)$, the Fourier transform of $h(r)$, however can be observed in scattering experiments.

$$S(Q) = 1 + \rho \int d\mathbf{r} h(r) \exp(-i\mathbf{Q}\mathbf{r}) = 1 + \rho\tilde{h}(Q) = \frac{1}{1 - \rho\tilde{c}(Q)}. \tag{20}$$

The correlation functions do not only provide information about the structure of the system. Thermodynamic quantities like pressure, internal energy and compresibility can also be obtained from integrals which contain the correlation functions. Statistical mechanics provides three different possibilities to calculate the thermodynamic properties: the virial route, the compressibility route and the energy route. Because of the approximations, introduced in the closure relation, the correlation functions are not exact and therefore the different routes have different results. This phenomenon is called thermodynamic inconsistency.

In order to work out the phasediagram, we used the following relations to calculate the pressure P via the virial route and the free energy F via the energy route for the liquid phase:

$$\frac{\beta P}{\rho} = 1 - \frac{2\pi\rho}{3} \int_0^\infty r^3 \beta\Phi'(r) g(r)\, dr \tag{21}$$

with $\Phi'(r) = \frac{d\Phi(r)}{dr}$. The free energy is obtained via the following expression:

$$\frac{\beta F}{N} \equiv f = f_{\text{id}} + f_{\text{ex}} \tag{22}$$

with

$$f_{\text{id}} = \ln\rho - 1 + 3\ln(\Lambda) \tag{23}$$

and

$$f_{\text{ex}} = 2\pi\rho \int dr r^2 \beta\Phi(r) \int_0^1 d\lambda g^\lambda(r;\rho). \tag{24}$$

Λ is the thermal de Broglie wavelength and $g^\lambda(r;\rho)$ is the pair correlation function of a system where particles interact via the scaled potential $\lambda\Phi(r)$. For calculations of the phase coexistence the last term in (23) can be dropped, since it also appears in the expression of the free energy of the solid phase.

The compressibility route provides access to the thermodynamic properties via the isothermal compressibility χ_T, which is given by

$$\chi_T = -\frac{1}{V}\left(\frac{\partial V}{\partial P}\right)_T \tag{25}$$

One can show that it is related to the correlation functions via

$$\frac{\rho\chi_T}{\beta} = 1 + \rho\int d^3\mathbf{r}[g(\mathbf{r}) - 1] = 1 + \rho\tilde{h}(0), \tag{26}$$

or, in terms of $\tilde{c}(Q)$

$$\frac{\beta}{\rho\chi_T} = 1 - \rho\tilde{c}(0). \tag{27}$$

3.2.1 IET for bounded potentials

The liquid phase for the PSM has been investigated extensively in literature, employing a wide variety of different closure relations [7][5][4]. In these contributions it has been found, that the Percus-Yevick and the hypernetted chain approximations fail to reproduce the process of clustering correctly. This phenomenon occurs indeed already at densities that are far below the freezing densities and thus in the liquid phase, where the cluster size ranges from one to several particles. Although this process of clustering in the liquid phase is still poorly understood from the theoretical point of view, it is undoubtedly observerd in Monte Carlo simulations.

This section is based on a theory developped by Likos *et al.*[4]. These authors could show, that for sufficiently high densities, MSA is the best closure for soft potentials in general . The validity of MSA for soft potentials is based on the assumption that at high densities many particles overlap and the average distance between the particles becomes vanishingly small. Thus every particle interacts with a huge number of others. The MSA provides accurate results for temperatures $T^* > 3.0$ and still fairly good results for $T^* > 2$. For lower temperatures the MSA breaks down.

The mean spherical approximation - MSA

The MSA closure was originally introduced for potentials, that consist of a hard core $\Phi_{\mathrm{HC}}(r < R) = \infty$ and an adjacent tail interaction $\Phi_{\mathrm{t}}(r > R)$, R being the hard core diameter. For those systems the MSA closure relation is given by:

$$c(r) = \begin{cases} -\beta\Phi_{\mathrm{t}}(r), & r > R \\ g(r) = 0, & r > R \end{cases} . \tag{28}$$

For bounded interactions like the PSM, no hard core exists and the MSA reduces to

$$c(r) = -\beta\Phi(r). \tag{29}$$

From equations (20) and (29) and introducing the Fourier transform of the potential, $\tilde{\Phi}(Q)$, we get the following analytic expressions for the static structure factor

$$S(Q) = \frac{1}{1 + \rho^*(T^*)^{-1}\tilde{\Phi}(Q)}. \tag{30}$$

The Fourier transform of the OZ equation reads as

$$\tilde{h}(Q) = \tilde{c}(Q) + \rho^*\tilde{h}(Q)\tilde{c}(Q). \tag{31}$$

Via equation (31) we obtain the following expression for the Fourier transform of the total correlation function $\tilde{h}(Q)$

$$\tilde{h}(Q) = \frac{(T^*)^{-1}\tilde{\Phi}(Q)}{1 + \rho^*(T^*)^{-1}\tilde{\Phi}(Q)}. \tag{32}$$

Equation (30) represents the basis for a criterion, that determines wether a systems will feature a cluster transition or re-entrant melting. Without going into details, the criterion states [4], that potentials with $\tilde{\Phi}(Q) > 0$ are members of the Q^+-class, which show a reentrant melting behaviour. Potentials with negative components in their Fourier transform form the $Q^{\pm}$-class, where cluster transitions are predicted.

Concentrating in the following on the $Q^{\pm}$ potentials we see from (30) that the static structure factor has a maximum when $\tilde{\Phi}(Q)$ attains its negative minimum value. $S(Q)$ even diverges, if

$$\frac{\rho^*}{T^*}|\tilde{\Phi}(Q^\star)| = 1, \tag{33}$$

where $Q^\star$ is the value of Q at which $\tilde{\Phi}(Q)$ reaches its minimum value. Equation (33) defines the spinodal line that confines the region where a liquid phase is stable (i.e. $\chi_T > 0$). Consequently, it can be concluded, that there is a fluid-solid transition at all densities.

Equation (30) can be used to qualitatively estimate the freezing line, employing the Hansen-Verlet criterion [19]. This empirical criterion states, that a system crystallizes, when the main peak of the static structure factor reaches a certain threshold value denoted by S_{HV}. The Hansen-Verlet criterion leads to the following estimate for the freezing line $T_f^*(\rho^*)$ via equation (30)

$$T_f^*(\rho^*) = \frac{\tilde{\Phi}(Q^\star)}{1 - S_{\mathrm{HV}}^{-1}}\rho^*. \tag{34}$$

This equation states that the slope of the freezing line is determined by the value of the Fourier transform of the potential at its first minimum value.

Calculation of the Pressure

For the PSM and the cmPSM the pressure can be evaluated analytically via the pressure route. For the PSM we find

$$\frac{\beta P}{\rho^*} = 1 + \frac{2\pi\rho^*}{3}[g(\sigma^+) - g(\sigma^-)], \tag{35}$$

where $g(\sigma^\pm)$ are the upper and lower limits of $g(r)$ at the core discontinuity. The analogous expression for the cmPSM reads as

$$\frac{\beta P}{\rho^*} = 1 + \frac{2\pi\rho^*}{3}[g(\sigma^+) - g(\sigma^-)] + \tau\kappa^3\frac{2\pi\rho^*}{3}[g(\kappa^+) - g(\kappa^-)], \tag{36}$$

where $g(\kappa^\pm)$ are the upper and lower limits of $g(r)$ at the inner core discontinuity and κ and τ are defined in section 2.2.

3.3 Density Functional Theory

The free energy calculations of the solid phase are based on density functional theory. In this case the free energy is a functional of the one-particle density $\rho = \rho(r)$.

It can be shown [12] that the free energy functional $F[\rho]$ has two important characteristics. Firstly, it is a unique functional of the one-particle density. Secondly, the functional has a lower bound equal to the true value of the free energy $F^\star$ of the system $F[\rho] \geq F^\star$ and the equilibrium density ρ_0 of the system minimizes the functional: $F[\rho_0] = F^\star$.

These two conditions provide the basis for a variational calculation of the free energy. What is additionally required is a format of the free energy functional $F[\rho]$ in terms of $\rho(\mathbf{r})$. An exact derivation of this format is impossible, except for trivial low dimensional systems. Therefore one has to rely an a approximate expression.

The free energy functional can be split into an ideal gas contibution and an excess part:

$$F[\rho] = F_{\mathrm{id}}[\rho] + F_{\mathrm{ex}}[\rho], \tag{37}$$

with

$$\beta F_{\mathrm{id}}[\rho] = \int d\mathbf{r}\rho(\mathbf{r})[\ln(\rho(\mathbf{r})\Lambda^3) - 1], \tag{38}$$

where Λ is the thermal de Broglie wavelength. For $F_{\mathrm{ex}}[\rho]$ we choose the mean field format, i.e.,

$$F_{\mathrm{ex}}[\rho] = \frac{1}{2}\int d\mathbf{r}\int d\mathbf{r}'\Phi(\mathbf{r},\mathbf{r}')\rho(\mathbf{r})\rho(\mathbf{r}'). \tag{39}$$

In many applications in soft matter systems this format has proved to give reliable results [20], [21]. In addition, recently reasons have been put forward by Likos *et al.* [6], why this format gives such good results for the solid phases in ultrasoft systems.

In our approach, the solid consists of a crystal of clusters, where the one-particle density profile of each cluster is assumed to take the form of a Gaus-

sian peak. The full one-particle density profile is the sum of these peaks over the whole lattice:

$$\rho(\mathbf{r}) = n_c \left(\frac{\alpha}{\pi}\right)^{\frac{3}{2}} \sum_{i=1}^{N_\mathrm{s}} \exp[-\alpha(\mathbf{r} - \mathbf{R}_i)^2]. \tag{40}$$

α is related to the width of the peaks. The prefactor guarantees the normalization condition $\int \rho(\mathbf{r}) d^3\mathbf{r} = N$, where N is the total number of particles and N_s is the number of lattice sites. The $\mathbf{R}_i$ are Bravais lattice vectors and each cluster incorporates n_c particles. Introducing a variable cluster size n_c allows multiple occupation of the Bravais lattice sites, which, dealing with clustering systems as the PSM, is to be expected.

We define $\alpha^* \equiv \alpha\sigma^2$. In the following we will drop the star.

Inserting the density profile (40) into the ideal and excess part of the free energy functional (39) turns the latter in a function that, for fixed number density ρ^* and temperature T^*, depends only on α and n_c, i.e.,

$$F[\rho] = F_\mathrm{id}[\rho] + F_\mathrm{ex}[\rho] = F(\alpha, n_c; \rho^*, T^*). \tag{41}$$

The ideal part can be approximated analytically, provided that the Gaussian peaks from different lattice sites do not overlap, leading to

$$\frac{\beta F_\mathrm{id}}{N} \equiv f_\mathrm{id} = \ln n_c + \frac{3}{2} \ln\left(\frac{\alpha}{\pi}\right) - \frac{5}{2} + 3 \ln\left(\frac{\Lambda}{\sigma}\right). \tag{42}$$

This approximation holds for reasonably large values of α. In the solid phase close to the coexistence region where the Gaussian density profile becomes broader and thus the overlap is growing, the integral has to be solved numerically. In our algorithm $\alpha = 30$ was used as the lower limit for above approximation.

The excess part reads as

$$\frac{\beta F_\mathrm{ex}}{N} \equiv f_\mathrm{ex} = \beta\Phi_E(0;\alpha) + \frac{n_c}{2} \sum_{\mathbf{R}_i} \beta\Phi_E(\mathbf{R}_i;\alpha), \tag{43}$$

with

$$\Phi_E(r;\alpha) = \begin{cases} \sqrt{\frac{\alpha^3}{2\pi}} \int_0^\infty dx\, x^2 e^{-\frac{\alpha}{2}x^2} \Phi(x) & r = 0 \\ \sqrt{\frac{\alpha}{2\pi}} \frac{1}{r} \int\limits_0^\infty dx\, x\, \Phi(x) \left[e^{-\frac{\alpha}{2}(x-r)^2} - e^{-\frac{\alpha}{2}(x+r)^2} \right] & r > 0 \end{cases} . \quad (44)$$

The term for $r = 0$ contains all interactions of particles from the same cluster, i.e., the intra-cluster contributions, whereas the term for $r > 0$ refers to the interactions of particles from different clusters, i.e., the inter-cluster contributions.

In the case of the PSM the integrals simplify to:

$$\Phi_E^{PSM}(r;\alpha) = \begin{cases} \sqrt{\frac{\alpha^3}{2\pi}} \int\limits_0^1 dx\, x^2 e^{-\frac{\alpha}{2}x^2} \epsilon & r = 0 \\ \sqrt{\frac{\alpha}{2\pi}} \frac{1}{r} \int\limits_0^1 dx\, x \left[e^{-\frac{\alpha^2}{2}(x-r)^2} - e^{-\frac{\alpha}{2}(x+r)^2} \right] \epsilon & r > 0 \end{cases} , \quad (45)$$

where for $r > 0$ the integral can even be solved analytically:

$$\begin{aligned} \Phi_E^{PSM}(r > 0;\alpha) &= \epsilon \left[\frac{e^{-\frac{\alpha}{2}(r+1)^2} - e^{-\frac{\alpha}{2}(r-1)^2}}{\sqrt{2\alpha\pi} r} \right] + \\ &+ \left\{ \frac{\mathrm{erf}[\sqrt{\frac{\alpha}{2}}(1-r)] + \mathrm{erf}[\sqrt{\frac{\alpha}{2}}(1+r)]}{2} \right\} . \end{aligned} \quad (46)$$

Collecting the terms (42)(45)(46) we obtain:

$$\begin{aligned} & f^{PSM}(\rho,\beta;\alpha,n_c) = f_{\mathrm{id}}^{PSM} + f_{\mathrm{ex}}^{PSM} = \quad (47) \\ = \;& \ln n_c + \frac{3}{2}\ln\left(\frac{\alpha}{\pi}\right) - \frac{5}{2} + \frac{1}{T^*}\sqrt{\frac{\alpha^3}{2\pi}} \int\limits_0^1 dx x^2 e^{-\frac{\alpha^2}{2}x^2} + \\ + \;& \frac{n_c}{2}\frac{1}{T^*} \sum_{\mathbf{R_i} \neq \mathbf{0}} \left\{ \frac{e^{-\frac{\alpha}{2}(r+1)^2} - e^{-\frac{\alpha}{2}(r-1)^2}}{\sqrt{2\alpha\pi} r} + \frac{\mathrm{erf}[\sqrt{\frac{\alpha}{2}}(1-r)] + \mathrm{erf}[\sqrt{\frac{\alpha}{2}}(1+r)]}{2} \right\} \end{aligned}$$

The last term in (42) has been dropped, since it also appears in the expression of the fluid free energy and therefore has no influence in the calculation of the phase coexistence region.

In the case of the cmPSM there are only a few changes to be made. While the expression for the ideal part of the free energy remains the same, the excess part now reads as

$$\Phi_E^{cmPSM}(r;\alpha) = \begin{cases} \sqrt{\frac{\alpha^3}{2\pi}} \int\limits_0^1 dx\, x^2 e^{-\frac{\alpha^2}{2}x^2} \tilde{\epsilon} & r = 0 \\ \sqrt{\frac{\alpha}{2\pi}} \frac{1}{r} \int\limits_0^1 dx\, x \left[e^{-\frac{\alpha^2}{2}(x-r)^2} - e^{-\frac{\alpha^2}{2}(x+r)^2} \right] \tilde{\epsilon} & r > 0 \end{cases} . \quad (48)$$

where $\tilde{\epsilon} \equiv [1-(1-\tau)\Theta(\kappa - x)]\epsilon$. κ and τ appearing in this equation are defined in section 2.2. Again, for $r > 0$ the integral can be solved analytically:

$$\begin{aligned} & \Phi_E^{cmPSM}(r>0;\alpha) = \epsilon \left[\frac{e^{-\frac{\alpha}{2}(r+1)^2} - e^{-\frac{\alpha}{2}(r-1)^2}}{\sqrt{2\alpha\pi} r} \right] + \\ + \quad & \epsilon \left\{ \frac{\mathrm{erf}[\sqrt{\frac{\alpha}{2}}(1-r)] + \mathrm{erf}[\sqrt{\frac{\alpha}{2}}(1+r)]}{2} \right\} - \\ - \quad & (1-\tau)\epsilon \left[\frac{e^{-\frac{\alpha}{2}(r+\kappa)^2} - e^{-\frac{\alpha}{2}(r-\kappa)^2}}{\sqrt{2\alpha\pi} r} \right] + \\ + \quad & (1-\tau)\epsilon \left\{ \frac{\mathrm{erf}[\sqrt{\frac{\alpha}{2}}(1-\kappa)] + \mathrm{erf}[\sqrt{\frac{\alpha}{2}}(1+\kappa)]}{2} \right\} . \end{aligned} \quad (49)$$

Adding the ideal part and the excess part leads to

$$\begin{aligned} & f^{cmPSM}(\rho,\beta;\alpha,n_c) \equiv f_{\mathrm{id}}^{cmPSM} + f_{\mathrm{ex}}^{cmPSM} = \\ = \quad & \ln n_c + \frac{3}{2}\ln\left(\frac{\alpha}{\pi}\right) - \frac{5}{2} + 3\ln\left(\frac{\Lambda}{\sigma}\right) + \\ + \quad & \frac{1}{T^*}\sqrt{\frac{\alpha^3}{2\pi}} \int\limits_0^1 dx\, x^2 e^{-\frac{\alpha^2}{2}x^2} [1-(1-\tau)\Theta(\kappa - x)] + \\ + \quad & \frac{1}{T^*} \sum_{\mathbf{R}_i \neq \mathbf{0}} \left\{ \left(\frac{e^{-\frac{\alpha}{2}(r+1)^2} - e^{-\frac{\alpha}{2}(r-1)^2}}{\sqrt{2\alpha\pi} r} + \frac{\mathrm{erf}[\sqrt{\frac{\alpha}{2}}(1-r)] + \mathrm{erf}[\sqrt{\frac{\alpha}{2}}(1+r)]}{2} \right) - \right. \\ - \quad & \left. (1-\tau) \left(\frac{e^{-\frac{\alpha}{2}(r+\kappa)^2} - e^{-\frac{\alpha}{2}(r-\kappa)^2}}{\sqrt{2\alpha\pi} r} + \frac{\mathrm{erf}[\sqrt{\frac{\alpha}{2}}(1-\kappa)] + \mathrm{erf}[\sqrt{\frac{\alpha}{2}}(1+\kappa)]}{2} \right) \right\} . \end{aligned} \quad (50)$$

The dependence on the density is now hidden in the lattice vectors. The lattice vectors $\mathbf{R_i}$ scale with the lattice constant a that is given by

$$a = \left(\frac{z n_c}{\rho} \right)^{\frac{1}{3}}, \tag{51}$$

where z is the number of particles in the unit cell, which is equal to 4 in the case of an fcc crystal.

Of course it is necessary to select a candidate lattice structure in order to calculate the sum in (47) or (50).

Minimizing the expression for the free energy (47) or (50) with respect to α and n_c gives the free energy for the solid at fixed ρ^* and T^*

$$f^\star(\rho, \beta) = \min_{\alpha, n_c} f(\rho, \beta; \alpha, n_c) = f^\star(\rho, \beta; \alpha^0, n_c^0). \tag{52}$$

α^0 and n_c^0 represent the values of α and n_c , which miminmize expression (52). A closer inspection of the contributions to the free energy in this minimization process is useful: in order to lower the free energy, on the one hand the logarithmic term in the ideal part and the prefactors of the sum in the excess part of the free energy favour low α. On the other hand, the exponentials in the excess part favour a high α which makes the existence of a local minimum plausible. It is not so obvious how the tendency to lower n_c is compensated. The answer is hidden in the sum over the lattice vectors in the inter-cluster term. From equation (51) it is clear that a low site occuppancy n_c means that the spacing between the lattice sites is narrow which in turn leads to more overlaps of the Gaussian peaks located at the lattice sites and thus to higher free energies.

The DFT-formalism outlined above gives information about the thermodynamics and the structure at any point (ρ^*, T^*) in the part of the phase diagram, where the solid phase is stable. In the fluid phase and in the coexistence region the formalism breaks down, indicating that there is no stable clustered phase to be found.

Using the free energies of the fluid phase, we can perform a common tangent construction in order to determine the phase boundaries between the solid and the fluid phases. Furthermore the formalism enables us to determine the equilibrium parameters of the density profile, i.e., the site occupancy n_c^0

and the width of the Gaussians α^0. Hence we can also predict the lattice constant via (51).

The expressions for the free energy can be equivalently derived from a Gibbs-Bogoljubov inequality using the Einstein model as a reference system for the crystal phase [22]. In the Einstein model the particles are considered to be tied to the lattice sites with springs.

3.3.1 Analytic methods

Likos *et.al* [6] suggested mean field approximation (MFA) for the thermodynamic properties of systems with bounded, repulsive interactions. It is beyond the scope of this section to reproduce the complete theory, instead we will restrict ourselves to some very useful considerations. The aim of these considerations is to predict the functional dependence of the parameters α and n_c on temperature and density.

Let $\{\mathbf{K}\}$ be a set of all reciprocal lattice vectors (RLVs). The RLVs are obtained according to a standard procedure, given e.g. by [23]. Moreover let $\mathbf{K} = \mathbf{K}\sigma$ be the dimensionless RLVs.

A Fourier transform of equation (39) leads to an expression for the free energy per particle of an ordered solid phase in terms of reciprocal lattice vectors $\mathbf{Y}$:

$$\frac{\beta F}{N}(\rho^*, T^*; n_c, \alpha) = \ln n_c + \frac{3}{2}\ln\left(\frac{\alpha}{\pi}\right) - \frac{5}{2} + \frac{\beta\rho}{2}\sum_{\mathbf{Y}} \tilde{\Phi}(Y)\exp\left(-\frac{Y^2}{(2\alpha)}\right), \quad (53)$$

where $Y = |\mathbf{Y}|$. Only n_c and α are variational parameters. The sum extends over all reciprocal lattice vectors, starting with the first shell of nearest neighboars in the reciprocal lattice. The advantage of this expression for the free energy over the equivalent expression in real space is, that it contains a discrete sum instead of the integrals. The sum can be truncated at some point, since both the Fourier transform of the potential and the exponential decay with increasing Y. Up to which lattice shell the terms of the sum have to be taken into account, depends on the specific form of the potential as well as on the lattice.

The first shell of RLVs are related to the lattice constant of the real space according to $K_1 = \zeta/a$, where ζ is a lattice dependent constant. Via equation (51) we obtain the following expression for the first dimensionless RLVs

$$Y_1(n_c) = \zeta \left(\frac{\rho^*}{z n_c} \right)^{1/3}. \tag{54}$$

Minimization of expression (53) above with respect to n_c and α leads to

$$\frac{T^*}{\rho^*} - \frac{1}{6} \sum_{\mathbf{Y} \neq 0} Y \left[\frac{\partial \tilde{\Phi}(Y)}{\partial Y} - \frac{Y}{\alpha^*} \tilde{\Phi}(Y) \right] \mathrm{e}^{-Y^2/(2\alpha^*)} = 0, \tag{55}$$

and

$$\frac{T^*}{\rho^*} + \frac{1}{6\alpha^*} \sum_{\mathbf{Y} \neq 0} \tilde{\Phi}(Y) Y^2 \mathrm{e}^{-Y^2/(2\alpha^*)} = 0. \tag{56}$$

All vestors Y scale with the first RLV Y_1, the scaling factor being a lattice dependent constant. Therefore the above conditions (55) and (56) constitute a nonlinear system of two equations in α and Y_1. Note, that the temperature and the density appear only in the ratio $\frac{T^*}{\rho^*}$ but not seperately. Letting α^0 and Y_1^0 represent the values of α and Y that solve the above system of equations, we conclude that both α^0 and Y^0 have to be functions of the ratio $\frac{T^*}{\rho^*}$.

$$\alpha^0 = \alpha^0(T^*/\rho^*), \tag{57}$$
$$Y_1^0 = Y_1^0(T^*/\rho^*), \tag{58}$$

and therefore

$$a = a(T^*/\rho^*). \tag{59}$$

We can make a second observation, which concerns the first RLV Y_1. For this purpose we subtract equation (56) from equation (55), which leads to

$$\sum_{\mathbf{Y} \neq 0} \frac{\partial \tilde{\Phi}(Y)}{\partial Y} Y e^{-Y^2/(2\alpha)} = 0. \tag{60}$$

Let the sum be truncated after the n-th shell and consider the high density limit $\alpha \to \infty$. In this limit, the exponentials become delta-functions and equation (60) above reduces to the following expression

$$\sum_{\mathbf{Y}\neq 0}^{\mathbf{Y}_n} \frac{\partial\tilde{\Phi}(Y)}{\partial Y} Y = 0, \tag{61}$$

where all RLVs Y scale with the first RLV Y_1. Let the solution of equation (60) be denoted by Y_1^*. Since neither the temperature nor the density do appear in the equation, Y_1^* has to be a lsystem-specific and lattice-specific universal constant.

Consequently we find, that there is a lower bound for the lattice constant a, namely

$$a_{min} = \zeta Y_1^*. \tag{62}$$

Thus, DFT predicts, that at high densities the lattice constant reaches a limiting value, which is universal for a specific potential type and lattice structure.

3.4 Monte-Carlo simulations

Monte Carlo (MC) simulations are a very important tool in condensed matter theory because they provide semi experimental data for a wide variety of observables in a thermodynamic system. As in our case, the data can be then used to check theoretical results. For technical reasons the size of the investigated systems is restricted to several thousands of particles, typically. Naturally, this number is far from macroscopic ensembles and there is no general guarantee that the properties of a physical, infinitly large system are reproduced correctly due to finite size effects.

3.4.1 Fundamentals

A typical MC simulation of a system of N particles with given interactions includes the following steps:

- An initial configuration is created by randomly assigning an initial position to all particles.
- A new configuration is generated from the preceding one by applying a trial move.
- The new configuration is subjected to an acceptance test, which has a specific design.
- Repeating the second and third step yields a sequence of configurations μ, which contains accepted configurations only. If a trial configuration fails the test, it is simply rejected and the 'old' configuration is added to the sequence instead.

An observable A is then obtained by averaging it over all n configurations in the sequence. Because of the lack of momenta in the model only static observables, such as the internal energy, the pair correlation function or the excess chemical potential, can be obtained directly in an MC simulation

$$\langle A \rangle = \frac{1}{n} \sum_{\mu=1}^{n} A(\mathbf{r}_\mu^N). \tag{63}$$

In a canonical ensemble with fixed N, V and T and the Hamilton function $H(\mathbf{p}^N, \mathbf{r}^N) = H_{\text{kin}}(\mathbf{p}^N) + V(\mathbf{r}^N)$, the ensemble average reduces to the configurational part, i.e.,

$$\langle A \rangle = \int d\mathbf{r}^N A(\mathbf{r}^N) f(\mathbf{r}^N), \tag{64}$$

where $f(\mathbf{r}^N) = \frac{\exp[-\beta V(\mathbf{r}^N)]}{Z}$ is the canonical probability density function and $Z \equiv \int d\mathbf{r}^N \exp[-\beta V(\mathbf{r}^N)]$ the configurational part of the partition function.

Comparing equations (63) and (64) we see, that (63) is an approximation or estimator of (64), if the sequence of configurations μ generated in the simulation samples the configuration space according to the probability density $f(\mathbf{r}^N)$. In other words, the probability p_μ of finding configuration μ in the sequence must equal the probability of finding it in configuration space:

$$p_\mu = f(\mathbf{r}_\mu^N) = \frac{\exp[-\beta V(\mathbf{r}_\mu^N)]}{Z} \equiv \frac{\exp(-\beta V_\mu)}{Z} \tag{65}$$

The key question is, how the algorithm, that generates new configurations, and the acceptance test must be designed, such that the configurations μ in the sequence are distributed according to equation (65).

3.4.2 Markov processes

The answer is best understood within the theoretical framework of a Markov process [24]. Consider the configurations as random variables or random states. Let q_μ^i be the probability of finding the system in state μ at the i-th position of the sequence and let $P_{\nu\mu}$ be the transition probability that state μ is transferred into state ν. In the MC simulation $P_{\nu\mu}$ incorporates the trial move and the acceptance test. A Markov process is characterized by:

$$q_\nu^{i+1} = \sum_\mu P_{\nu\mu} q_\mu^i, \tag{66}$$

with

$$\sum_{\mu\nu} P_{\nu\mu} = 1. \tag{67}$$

Expression (66) can be rewritten as a matrix equation

$$\mathbf{q}^{i+1} = \mathbf{P} \cdot \mathbf{q}^i, \tag{68}$$

with $\mathbf{q} = \{q_\mu^i\}$ and $\mathbf{P} = \{P_{\nu\mu}\}$. Starting from an initial distribution $\mathbf{q}^0$, $\mathbf{q}^i$ is obtained by repeated action of $\mathbf{P}$.

$$\mathbf{q}^i = \underbrace{\mathbf{P} \ldots \mathbf{P}}_{i-\text{times}} \cdot \mathbf{q}^0 \equiv \mathbf{P}^i \cdot \mathbf{q}^0. \tag{69}$$

Next we impose two conditions on the transition probabilities $\mathbf{P}$, that are closely related to two concepts of statistical mechanics. In the framework of statistical mechanics, ergodicity means that a system approaches every point n phase space deliberately close after a finite amount of time, regardless of the starting point. We can apply an analogous concept to the Markov chain: A Markov chain is said to be ergodic, if any distribution $\mathbf{q^i}$ can be reached after a finite number of steps i, regardless of the initial distribution $\mathbf{q}^0$. The second condition postulates the existence of an equilibrium distribution $\mathbf{p}$ which satisfies:

$$\mathbf{p} = \mathbf{P} \cdot \mathbf{p}, \tag{70}$$

or, in component form:

$$p_\nu = \sum_\mu P_{\nu\mu} p_\mu. \tag{71}$$

In order to establish the correct relation to statistical mechnaics (65), in the case of interest the equilibrium probability distribution p_μ should equal the probability density function of the canonical ensemble:

$$p_\mu = \frac{\exp(-\beta V_\mu)}{Z}. \tag{72}$$

Provided that the chain is ergodic, it can be shown that such an equilibrium exists, if the transition probabilities satisfy the condition of microscopic reversibility:

$$p_\nu P_{\mu\nu} = p_\mu P_{\nu\mu}, \tag{73}$$

or

$$\frac{p_\nu}{p_\mu} = \frac{P_{\mu\nu}}{P_{\nu\mu}}. \tag{74}$$

This relation expresses the fact, that on average a transition from state μ to state ν occurs as often as in the opposite direction.

3.4.3 The Metropolis Method

The task of finding ergodic transition probabilities $P_{\nu\mu}$, which satisfy microscopic reversibility (73), and equation (72), is simplified by introducing a selection probability $s(\mu \to \nu)$ that incorporates the creation of a new configuration and an acceptance ratio $a(\mu \to \nu)$ that incorporates the acceptance test

$$P_{\mu\nu} = s(\mu \to \nu)a(\mu \to \nu). \tag{75}$$

The Metropolis algorithm [25] yields a particularly effective and simple way of defining s and a.

Trial moves

In a canonical ensemble $s(\mu \to \nu)$ is usually effected by a trial move of a randomly chosen particle i:

$$\mathbf{r}_i \to \mathbf{r}_i + \Delta\xi_i, \tag{76}$$

where the $\xi_i \in [-1, 1]$ are uniformly distributed random numbers and Δ is an arbitrarily chosen displacement constant. This choice of $s(\mu \to \nu)$ allows a particle to reach any point in the box and hence is ergodic. Furthermore the condition

$$s(\mu \to \nu) = s(\nu \to \mu) \tag{77}$$

is clearly guaranteed.

Acceptance rate

Equations (74), (75) and (77) yield

$$\frac{p_\nu}{p_\mu} = \frac{P_{\mu\nu}}{P_{\nu\mu}} = \frac{s(\mu \to \nu)a(\mu \to \nu)}{s(\nu \to \mu)a(\nu \to \mu)} = \frac{a(\mu \to \nu)}{a(\nu \to \mu)}, \tag{78}$$

and with the specific form (72) of the probability distribution p_ν

$$\frac{a(\mu \to \nu)}{a(\nu \to \mu)} = \frac{p_\nu}{p_\mu} = \frac{\exp(-\beta V_\nu)}{\exp(-\beta V_\mu)} = \exp[-\beta(V_\nu - V_\mu)]. \tag{79}$$

In the Metropolis algorithm $a_(\mu \to \nu)$ is set to:

$$a(\mu \to \nu) = \begin{cases} \exp[-\beta(V_\nu - V_\mu)] & V_\nu - V_\mu > 0 \\ 1 & else \end{cases} \tag{80}$$

This choice of $a(\mu \to \nu)$ fulfills equation (72) and provides the highest possible acceptance ratios.

As far as the acceptance ratios, i. e. the ratio between accepted and proposed moves, are concerned, they should in practice range somewhere between $30\% - 60\%$. A high acceptance ratio on the one hand indicates that the trial moves hardly change the configuration. A low acceptance ratio on the other hand means, that few configurations are available to calculate the ensemble averages. In both cases the system proceeds very slowly on its random way through the phase space.

In a Metropolis algotithm the displacement Δ plays the role of a tuning parameter which can be used to optimize the acceptance ratio.

3.4.4 Calculation of the free energy - Widom method

The free energy of a system can not be recovered directly from an MC simulation. Instead, a method proposed by Widom [26] has turned out to be very effective for the calculation of the free energy, because it can be implemented in a standard Metropolis simulation. From thermodynamics we know the following Gibbs-Duhem relation:

$$F = -PV + \mu N. \tag{81}$$

The pressure P can be obtained from the pair correlation function $g(r)$ via the virial route (35),(36). Hence we focus on the chemical potential μ, which

in a canonical ensemble with fixed N V and T is given by

$$\mu = \left(\frac{\partial F}{\partial N}\right)_{V,T}. \tag{82}$$

For sufficiently large N this expression can be approximated by

$$\mu \cong F(N+1,V,T) - F(N,V,T). \tag{83}$$

The classical partition function reads as

$$Q(N,V,T) = \frac{1}{\Lambda^N N!}\int_V d\mathbf{r}^N \exp[-\beta V(\mathbf{r}^N)], \tag{84}$$

where Λ is the thermal de Broglie wavelength. The free energy is given by

$$\begin{aligned} F &= -k_B T \ln Q = -k_B T \ln\left(\frac{1}{\Lambda^N N!}\right) - \\ &- k_B T \ln\left[\int_V d\mathbf{r}^N \exp[-\beta V(\mathbf{r}^N)]\right]. \end{aligned} \tag{85}$$

Conbining equations (83) and (85) yields

$$\mu = -k_B T \ln\left(\frac{1}{\Lambda^3(N+1)}\right) - k_B T \ln\left[\frac{\int d\mathbf{r}^{N+1}\exp[-\beta V(\mathbf{r}^{N+1})]}{\int d\mathbf{r}^N \exp[-\beta V(\mathbf{r}^N)]}\right] \equiv \mu_{\rm id} + \mu_{\rm ex}. \tag{86}$$

The first term in (86), denoted by $\mu_{\rm id}$ is the ideal gas part, that can be calculated analytically. The second or excess part can be rewritten as an ensemble average:

$$\begin{aligned} &\mu_{\rm ex} = -k_B T \ln\left[\frac{\int d\mathbf{r}^{N+1}\exp[-\beta V(\mathbf{r}^{N+1})]}{\int d\mathbf{r}^N \exp(-\beta V(\mathbf{r}^N))}\right] = \\ &= -k_B T \ln \int d\mathbf{r}^{N+1}\left[\exp[-\beta V(\mathbf{r}^{N+1}) - \beta V(\mathbf{r}^N)]\right]\frac{\exp[-\beta V(\mathbf{r}^N)]}{\int d\mathbf{r}^N \exp[-\beta V(\mathbf{r}^N)]} = \\ &= -k_B T \ln \int d\mathbf{r}^{N+1}\exp(-\beta\Delta V) f(\mathbf{r}^N). \end{aligned} \tag{87}$$

The last line of above relation expresses μ_{ex} as a canonical ensemble avarage of $\exp(-\beta\Delta V)$ in a system of N particles, which is exactly the form we need, in order to derive an observable from an MC simulation. $\Delta V \equiv \beta[V(\mathbf{r}^{N+1}) - V(\mathbf{r}^N)]$ is the interaction energy of the inserted particle (index $N+1$) with the rest of the system.

In practice, the measurement of ΔV is implemented in the standard Metropolis algorithm in the following way:

- Insert one particle at a random position in a given configuration.
- Calculate the interaction energy ΔV of the inserted particle with all other particles.
- Let the Metropolis algorithm go on and repeat the procedure at selected intervals.

The chemical potential is then obtained by avaraging over all particle insertions. Of course there is no acceptance test, because the insertions are never accepted and thus have no influence whatsoever on the course of the simulation.

Usually this method is limited to low density regions. At high densities or in the solid phase, there is simply no space, where the 'ghost'-particle could be inserted. This problem does not occur with soft potentials as the PSM. since in this case, the particles are allowed to fully overlap and an insertion is possible at all densities.

In order to test the particle insertion method, we used the overlapping distribution method [13].

3.4.5 Boundary Conditions and System Parameters

As already mentioned in the introduction to this chapter, the size of a simulized system is restricted due to limited computational capacities. Problems arise from the inevitably large surface to volume ratio. Out of thousand particles, which are confined in a cubic box almost half of them are surface atoms. Since we are interested in the bulk properties of a system, these surface atoms make flawed contributions to the observables.

Unwanted surface effects can be partially encountered, by imposing specific boundary conditions on the system: Consider a ensemble of N particles in

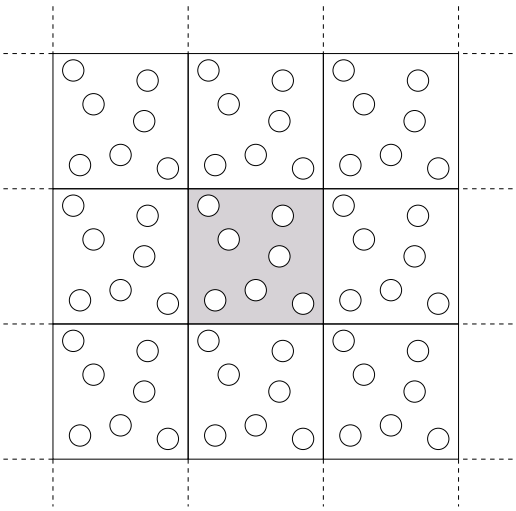

Figure 4: An illustration of the concept of periodic boundary conditions. All boxes are copies of the original box and the duplicated particles have the same positions and momenta with respect to their boxes

a cubus of volume V. In order to compensate the finite size of the system, the cubus or box is duplicated as shown in Figure 4. All boxes are copies of the original box and all duplicated particles have the same positions and momenta with respect to their boxes. If a particle leaves a box it returns from the opposite edge with its momentum left unchanged, thus keeping the system balanced. This concept is known as periodic boundary condition.

For ordered systems there is a particular finite size effect of practical importance, that can not be overcome with periodic boundary conditions. A crystal is only stable if its geometry is compatible to the one of the simulation box. Consider a system, that freezes at a certain temperature and density, forming an fcc lattice with corresponding lattice constant. If the box length is not a multiple of the lattice constant, high surface energies at the boundary edges of the box will prevent the system from freezing or make it melt, if it was initially crystallized. Therefore the particle number N has to be adjusted in such a way, that the crystal lattice 'fits' the box. In the case of an fcc-lattice:

$$N = 4n^3, \qquad \text{where} \qquad n \in \{1, 2, 3, 4, ...\} \tag{88}$$

In a clustering system like the PSM, there are more than one particles located at each lattice site and equation (88) becomes

$$N = 4n^3 n_c, \qquad n \in \{1, 2, 3, 4, ...\} \tag{89}$$

with the site occupancy n_c. Consequently, the site occupancy has to be estimated before the MC-simulation can be started, otherwise we would not be able to determine the number of particles. For this purpose we used the results from density functional theory.

Usually the interaction potential of a system is long-range, and has to be truncated at a radius smaller than half the box length. The contributions to the interaction from outside this radius are approximated in a background correction term. This concept is called the nearest-image convention.

Fortunately the PSM has a model-immanent cutoff τ and the interactions can be calculated without any corrections.

3.4.6 Technical Details

The Monte-Carlo simulations in this work were carried out using a standard Metropolis algorithm. For the simulations in the liquid phase, a particle number $N = 1000$ was used. The initial configuration was generated by assigning a random position to every particle.

For the simulations in the solid phase, the particle number of the system was chosen according to equation (89). The results from DFT provided an estimate for the site occupancy n_c. The initial configuration for simulations in the solid phase was generated as follows: First, an fcc lattice with 108 or 256 lattice sites was generated. Next, n_c particles were placed at each lattice sites. The number of lattice sites was chosen in such a way that the total particle number never exceeded the amount of 5000 particles.

Starting from the initial configuration, the system was allowed to equilibrate for 50000 passes, where a pass consists of N trial moves, i.e., on avarage each particle has been subjected to a trial move once in each pass. After the equilibration, the ensemble averages were calculated, letting the system run for another 100000 passes.

The quantities that are derived directly from the simulations are the pair correlation function $g(r)$ and the free energy F via the Widom method (see section 3.4.4). In the solid phase the shape of the clusters is analyzed, i.e., the one-particle density profile. The site occupancy n_c and thus the lattice constant a are fixed according to the estimates from DFT and do not change

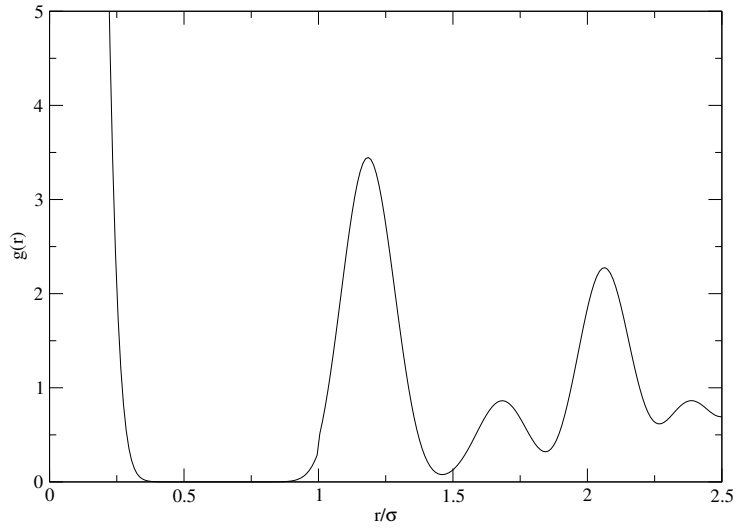

Figure 5: The pair correlation function $g(r)$ for the PSM at temperature $T^* = 3.0$ and density $\rho^* = 20.0$. In the calculations of the shape and size of the clusters in the solid phase the particle diameter R was set to equal the position of the first minimum of the pair correlation function. In the case of the PSM we chose $R/\sigma = 0.7$.

in the course of the simulation. Therefore a comparison of these quantities to DFT would be tautological.

One specific problem occurred in the solid phase, namely two clusters were sometimes counted as one, due to a marginal overlap. A double cluster makes flawed contributions to the data, that is measured in the course of the simulation. The calculation of the centers of mass is affected as well as the measurement of the mean cluster size and the calculation of the shape of the clusters. In order to avoid this problem the particle diameter was reduced and set to equal the first minimum of the pair correlation function $g(r)$ in all calculations related to the shape and size of the clusters in the solid phase. Figure 5 shows a typical pair correlation function in the solid phase of the PSM.

3.5 Fluid-Solid Transitions

Common Tangent Construction According to the Ehrenfest classification, the fluid-solid transition is a a first-order phase transition, because it involves a discontinous change of the density, which is a first derivative of the free energy. A first-order transition is always associated with a coexistence region, i.e., a region, where the solid and liquid phase coexist. The coexistence region of a system at a given temperature can be determined with the help of a common tangent construction, exploiting the fact, that at given temerature two coexisting phases, liquid and solid have equal pressures and chemical potentials:

$$P_{\text{liq}}(\rho_{\text{liq}}) = P_{\text{sol}}(\rho_{\text{sol}}) \tag{90}$$
$$\mu_{\text{liq}}(\rho_{\text{liq}}) = \mu_{\text{sol}}(\rho_{\text{sol}}). \tag{91}$$

Both P and μ can be expressed in terms of free energy per volume $\tilde{f}(\rho) = \frac{F(\rho)}{V}$:

$$P = -\left(\frac{\partial F}{\partial V}\right)_N = -\frac{\partial[\tilde{f}(\rho)V]}{\partial V} = \rho\frac{\partial \tilde{f}(\rho)}{\partial \rho} - \tilde{f}(\rho) \tag{92}$$
$$\mu = \left(\frac{\partial F}{\partial N}\right)_P = \frac{\partial[\tilde{f}(\rho)V]}{\partial N} = \frac{\partial \tilde{f}(\rho)}{\partial \rho}. \tag{93}$$

The points $(\rho_{\text{liq}}, \tilde{f}(\rho_{\text{liq}})$ and $(\rho_{\text{sol}}, \tilde{f}(\rho_{\text{sol}})$ which fulfill the conditions (92) (93) define the boundaries of the coexistence region at a given temperature.

Lindemann criterion At finite temperature, particles in a crystal are not fixed to their lattice sites but oscillate around their equilibrium position. In a simple approximation the particles can be viewed as tied to their sites with springs, where the mean distance r to their equilibrium position is estimated by the root-mean-square displacement $\sigma = \sqrt{\langle r^2\rangle - \langle r\rangle^2}$. The Lindemann criterion [27] now states, that if the ratio between the root-mean-square displacement and the nearest neighbour distance a_0 in the lattice reaches a critical upper limit, the crystal is no longer stable and melts. The criterion is empirical in nature and there are no universal critical values for

the Lindemann ratio. For typical pair interactions of soft matter and typical thermodynamic conditions the critical values range from $0.14 - 0.19$.

For the one-particle density profile given by (40), the root-mean-square displacement reads as $\sigma = \sqrt{3/2\alpha}$. In an fcc lattice with lattice constant a the nearest neighbours are located at a distance $a_0^{\text{fcc}} = \frac{\sqrt{2}a}{2}$. Recalling equation (51) we can write down the Lindemann ratio for an fcc crystal of clusters:

$$L = \sqrt{\frac{3}{\alpha}} \left(\frac{\rho}{4n_c} \right)^{\frac{1}{3}}. \tag{94}$$

4 Results

This section is organized as follows: First we examine the validity of the DFT by comparing the results for the free energies from Monte Carlo simulation and DFT, respectively. In the DFT formalism, that was used for the calculations of the solid phase, the following assumptions were made about the structure and the thermodynamics of the solid phase:

- The fcc lattice is a stable structure at all densities and temperatures in the solid phase.
- The clusters have the shape of Gaussians, according to the one-particle density given by (40).
- The format for the density functional (39) leads to reliable results for the free energy.

Once having justified the DFT formalism, we show the phase diagram as obtained by common tangent construction and the DFT results for the solid phase. Apart from the free energies of the solid phase, DFT yields also the equilibrium parameters of the density profile: α and the site occupancy n_c. The site occupancy n_c, in turn, yields the lattice constant a via equation (51). A key interest of this work was to find and interpret the dependence of these parameters on temperature and density.

In the discussion of the results, emphasis is put on the question, whether the numerical results meet the various theoretical predictions (see sectioon ()).

Throughout this section we will compare our results to those provided by recent theoretical [6] and numerical [20] investigations of the GEM-4 and discuss essential common features as well as the differences.

The results for the PSM and the cmPSM will be given in two seperate sections.

4.1 Results for the PSM

The liquid phase of the PSM

For all calculations of the liquid phase of the PSM we used the MSA closure in the framework of IET. Figures 6 to 8 show a comparison of the pair

correlation function $g(r)$ as obtained by IET and MC simulations. Figure 9 visualizes a typical configuration of a MC simulation.

The figures clearly reveal the fact, that already at densities where the fluid phase is stable, clustering occurs, though the clusters do not form an orderd lattice. The high values of the pair correlation function $g(r)$ at the origin reflect this phenomenon.

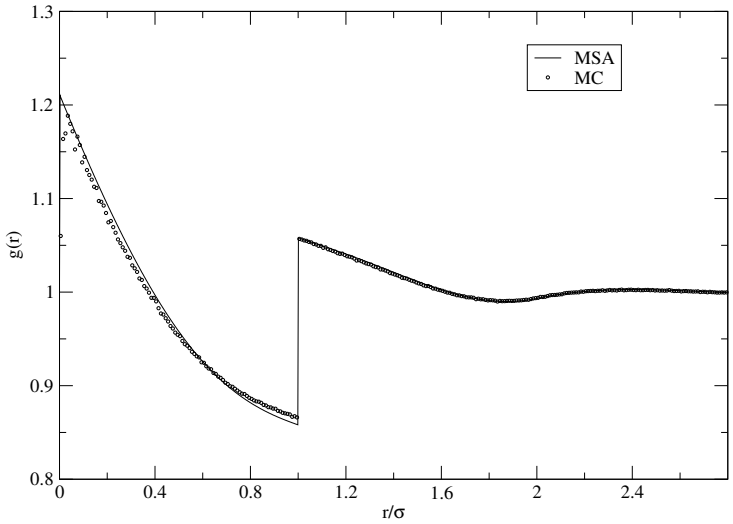

Figure 6: The pair correlation function $g(r)$ for the PSM at temperature $T^* = 5.0$ and density $\rho^* = 5.0$ as obtained from MC simulation and via MSA.

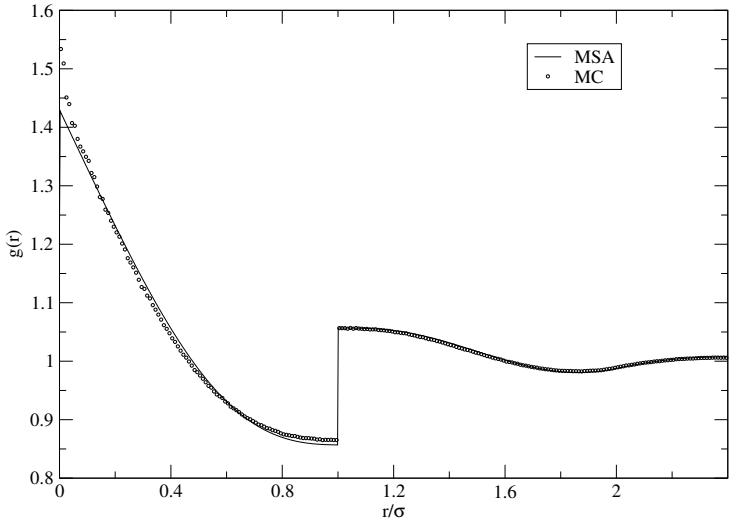

Figure 7: The pair correlation function $g(r)$ for the PSM at temperature $T^* = 5.0$ and density $\rho^* = 8.0$ as obtained from MC simulation and via MSA.

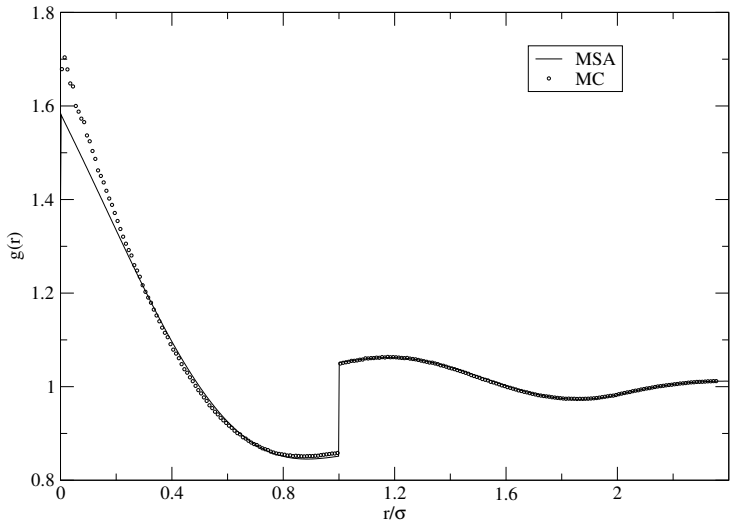

Figure 8: The pair correlation function $g(r)$ for the PSM at temperature $T^* = 5.0$ and density $\rho^* = 9.5$ as obtained from MC simulation and via MSA.

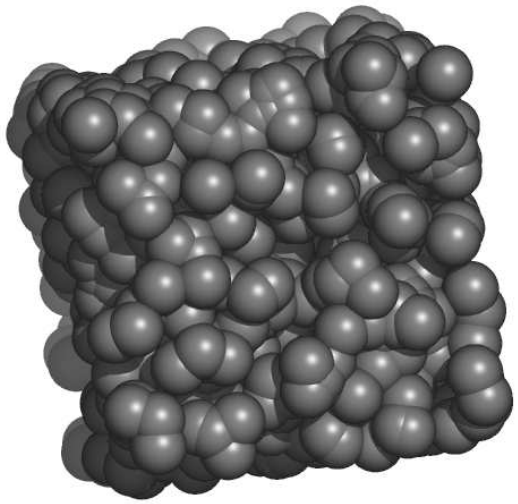

Figure 9: A simulation snapshot of the PSM at temperature $T^* = 5.0$ and density $\rho^* = 8.0$ in the fluid phase. This disorderd phase is formed by clusters of particles of variyble size.

Comparison to simulation

MC simulations have been performed along the isothermal $T^* = 3.0$ at densities

$$\rho^* = \{4.0,\ 6.0,\ 7.0,\ 12.0,\ 16.0,\ 20.0\}, \tag{95}$$

and along the isothermal $T^* = 5.0$ at densities

$$\rho^* = \{5.0,\ 6.5,\ 8.0,\ 9.5,\ 10.0,\ 10.2,\ 10.4,\ 10.6,\ 10.8,\ 14.0,\ 20.0\}, \tag{96}$$

(see Figure 20). Figure 10 shows the cluster pair correlation function, i.e., the pair correlation function of the centers of mass of the clusters, at densities $\rho^* = 12.0$ and $\rho^* = 16.0$ as obtained by MC simulations. It is clearly demonstrated, that the initial fcc structure remained stable throughout the simulation because the positions of the peaks of the cluster pair correlation functions match the respective positions of an ideal fcc lattice. Figure 11 shows a snapshot of a MC simulation at temperature $T^* = 3.0$ and density $\rho^* = 12.0$. The diameter of the particles is equal to the potential range σ. In Figure 12 a snapshot of the same simulation is shown, with a different, arbitrarily chosen particle diameter. Both snapshots clearly reveal the fcc structure.

The presumed Gaussian form of the density profile of the clusters $\rho_{\mathrm{cl}}(r)$ (40) was confirmed by the simulation results, as shown in Figures 13 to 15 for two different densities $\rho^* = 12.0$ and $\rho^* = 16.0$ at temperature $T^* = 3.0$. In the simulation results the statistics are very poor for low distances $r/\sigma < 0.1$ as well as for large distances $r/\sigma > 0.3$. Therefore the accordance of DFT and simulation is poor in this regions. Figures 14 and 16 show the density profile density as a function of r^2/σ^2 on a logarithmic scale for the intermediate range $0.1 < r/\sigma < 0.3$. The accordance is good and justifies the ansatz.

The results for the free energy in the solid phase provided by DFT were found to be in good accordance with the simulation results. Figures 17 and 18 show a comparison of the results of the two different methods for temperatures $T^* = 3$ and $T^* = 5$. The MSA closure in the framework of IET was used to calculate the free energies in the liquid phase.

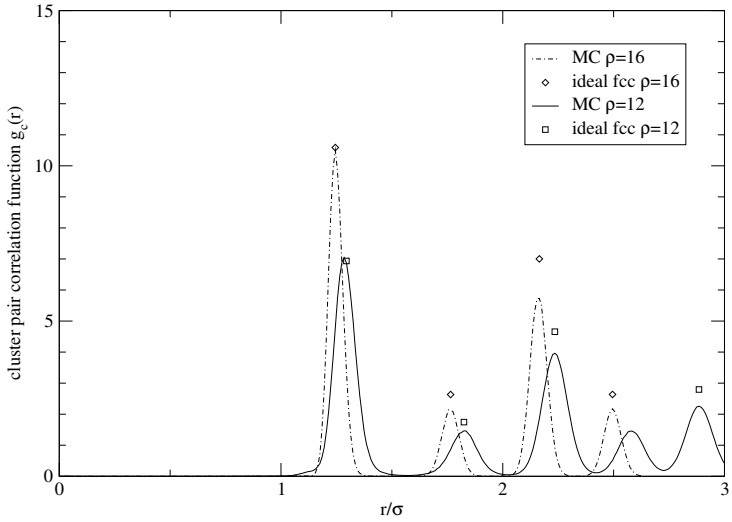

Figure 10: The cluster pair correlation function $g_c(r)$ at densities $\rho^* = 12.0$ and $\rho^* = 16.0$ as obtained by MC simulations at temperature $T^* = 3.0$. The diamonds and squares denote the positions of the peaks of the pair correlation function of an ideal fcc-lattice at the respective temperatures.

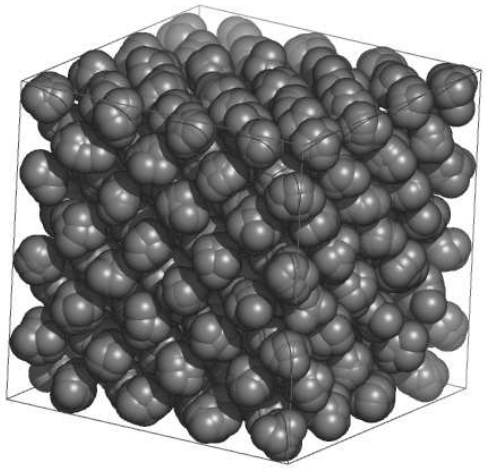

Figure 11: A snapshot of an MC simulation at $\rho^* = 12.0$ and $T^* = 3.0$. The size of the particles shown in the figure corresponds to the potential cutoff at $\sigma = 1$.

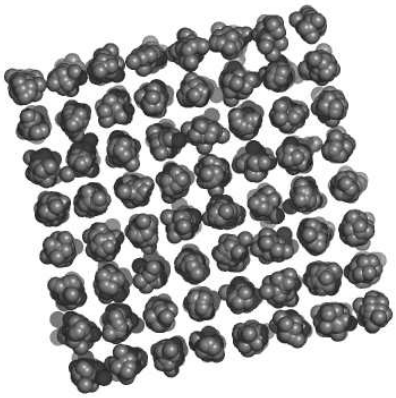

Figure 12: A snapshot of an MC simulation at $\rho^* = 12.0$ and $T^* = 3.0$. The size of the particles in the figure is arbitrarily chosen in order to display the lattice structure of the system in a better way.

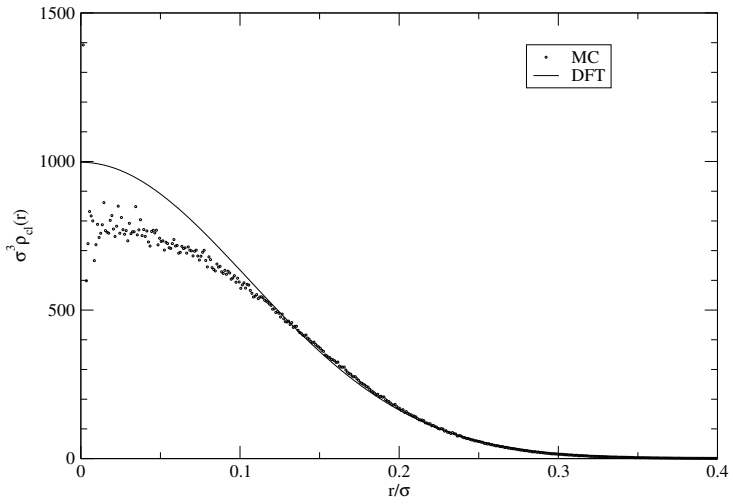

Figure 13: Comparison of the density profile of the clusters $\rho_{\mathrm{cl}}(r)$ in the solid phase as obtained by DFT and MC-simulation at $\rho^* = 12.0$ and $T^* = 3.0$.

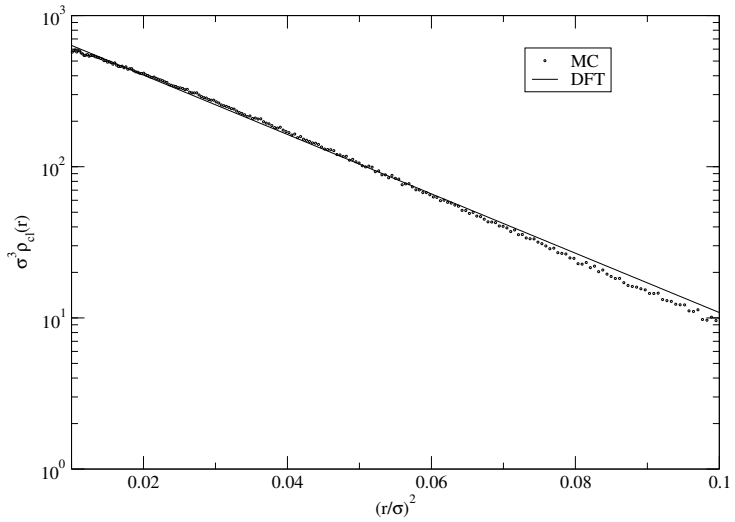

Figure 14: Comparison of the density profile of the clusters $\rho_{\mathrm{cl}}(r)$ in the solid phase as a function of r^2/σ^2 as obtained by DFT and MC-simulation at $\rho^* = 12.0$ and $T^* = 3.0$.

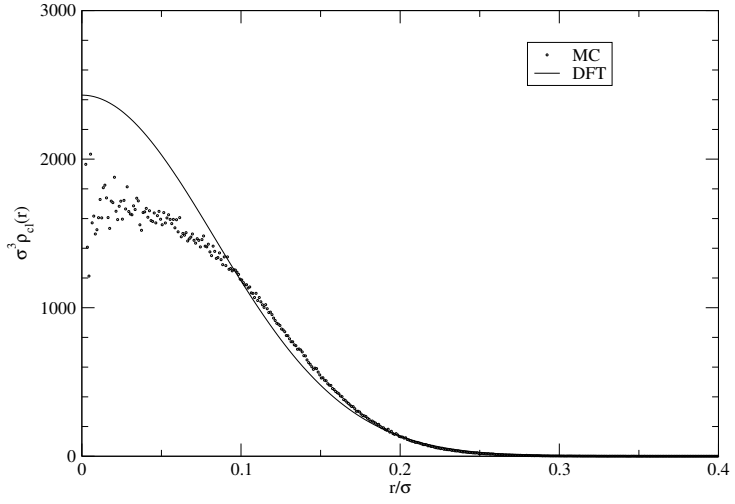

Figure 15: Comparison of the density profile of the clusters $\rho_{\mathrm{cl}}(r)$ in the solid phase as obtained by DFT and MC-simulation at $\rho^* = 16.0$ and $T^* = 3.0$.

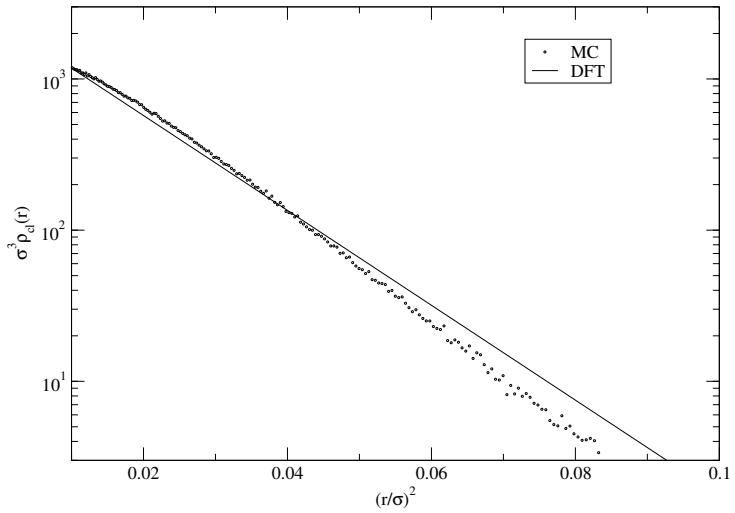

Figure 16: Comparison of the density profile of the clusters $\rho_{\mathrm{cl}}(r)$ in the solid phase as a function of r^2/σ^2 as obtained by DFT and MC-simulation at $\rho^* = 16.0$ and $T^* = 3.0$.

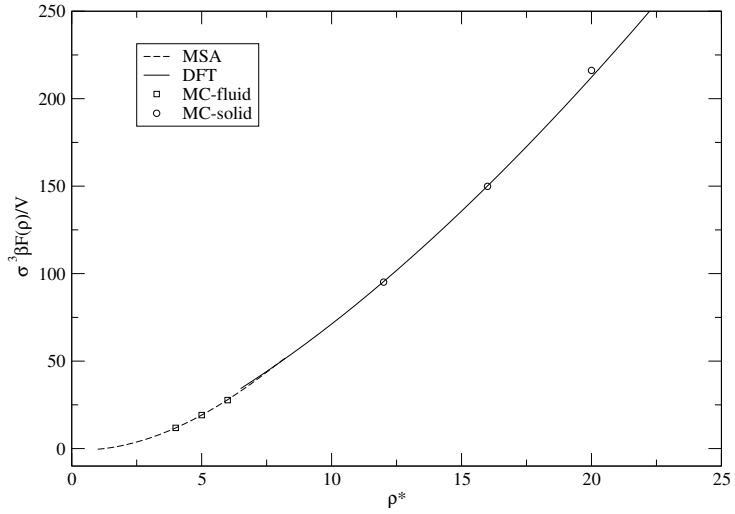

Figure 17: The free energy per volume $\sigma^3\beta F/V$ as a function of the reduced number density ρ^* at temperature $T^* = 5.0$. The circles denote results from MC simulations whereas the lines were obtained from DFT.

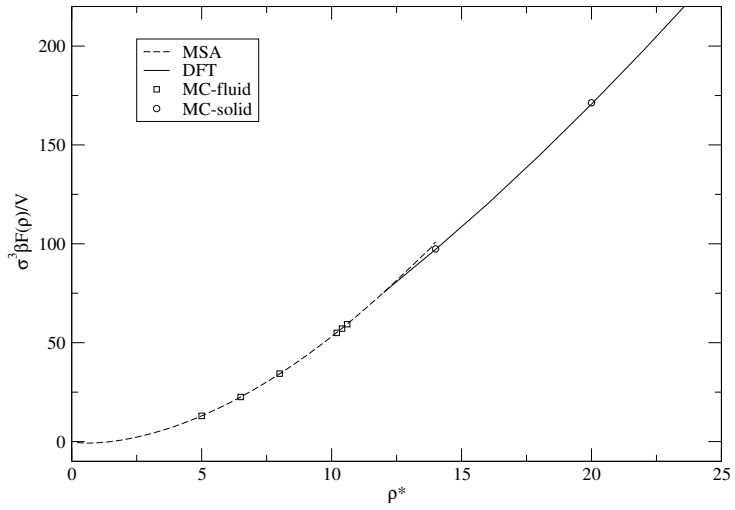

Figure 18: The free energy per volume $\sigma^3 \beta F/V$ as a function of the reduced number density ρ^* at temperature $T^* = 3.0$. The circles denote results from MC simulations whereas the lines were obtained from DFT.

4.1.1 The phase diagram of the PSM

In order to work out the phase diagram of the PSM a common tangent construction was performed for temperatures ranging from $T^* = 2.0$ to $T^* = 10.0$. The MSA closure in the framework of IET was used to calculate the free energies in the liquid phase and DFT was applied to calculate the free energies of the solid phase. The coexistence region was found to be wedge-shaped and the boundaries of the coexistence region are straight lines for temperatures $T^* > 3.0$. For lower temperatures, the boundaries of the coexistence region are inclined towards higher densities. From a theoretical point of view, this can be understood, by considering the low temperature limit $T^* \to 0$. It is clear that in this limit, the PSM is equivalent to a system of hard spheres, which undergoes a freezing transition at $\rho^* = 0.945$ [12]. In order to reach this value, the boundaries of the coexistence region at some point have to deviate from the wedge-like shape that prevails at high temperatures.

The same form of the coexistence region has been found for the GEM-4, between the fluid phase and a bcc structure, however, which is not present in the PSM. Compared to the GEM-4, the phase boundaries are steeper in the PSM. This means that if in the fluid phase, at a given temperature, the density is continuously increased, the PSM freezes earlier than its relative, the GEM-4. According to theory (see section 3.2.1), this behaviour was to be expected, since the value of the first minimum of the Fourier transform of the PSM is larger than the respective value of the GEM-4 (see Figure 21).

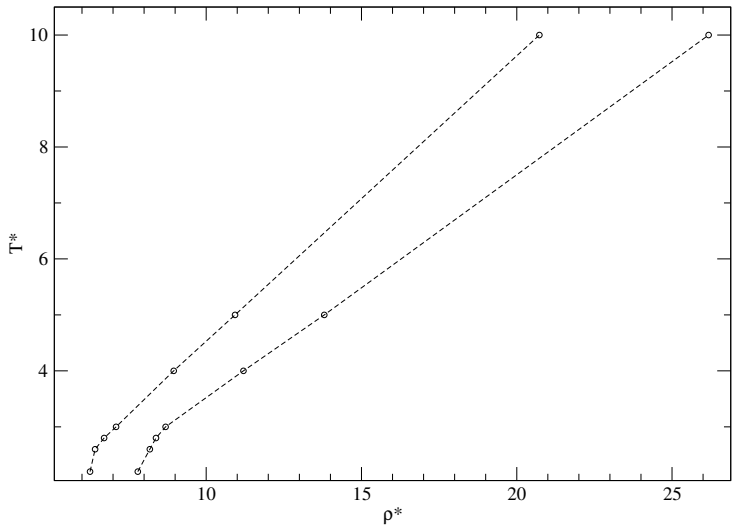

Figure 19: The phase diagram of the PSM in the (T^*, ρ^*)-plane. The lines confine the region where liquid and the solid phases coexist. The circles denote the data points, that were obtained from common tangent construction.

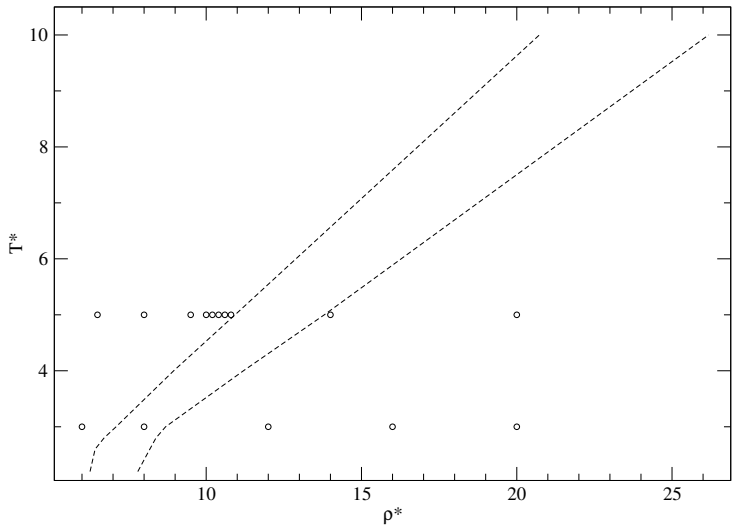

Figure 20: The same figure as 19. In this figure, the circles denote the points $\{\rho^*, T^*\}$ where MC simulations were performed.

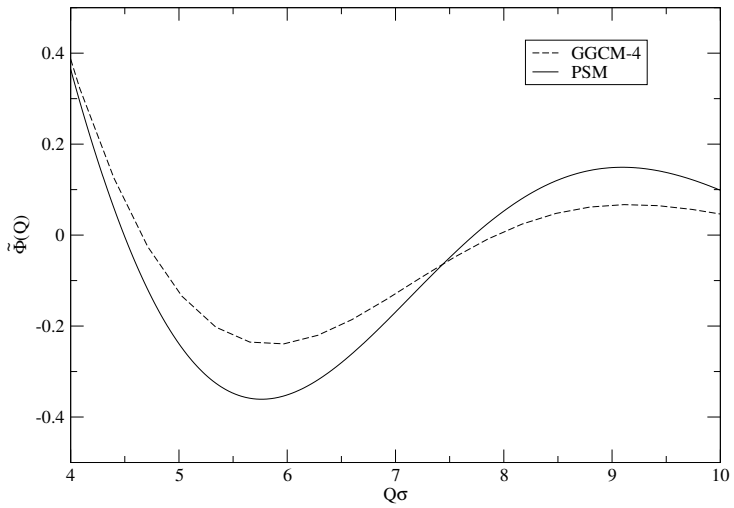

Figure 21: The Fourier transforms $\tilde{\Phi}(Q)$ of the PSM and the GEM-4. The value of the first minimum in $\tilde{\Phi}(Q)$ is $|\tilde{\Phi}(Q^\star)| = 0.37$ for the PSM and $|\tilde{\Phi}(Q^\star)| = 0.25$ for the GEM-4.

4.1.2 The solid phase of the PSM

As far as the lattice constant a is concerned, we found that the numerical results from DFT confirm the theoretical predictions: The lattice constant is a unique function of the ratio between density and temperature; at a fixed value of the ratio ρ^*/T^* the lattice constant attains the same value for all temperatures (see Figures 22 and 23). With increasing density, the lattice constant decreases. The higher the density, however, the more the curve flattens, asymptotically tending towards a lower bound. Physially spoken, at high densities, the lattice constant hardly changes, and any further increase of the density is compensated by an increase of the site occupancy. This is exactly the behaviour, that was predicted by theory (see section 3.3.1).

Regarding the site occupancy n_c, we intuitively expect it to increase with increasing density. In the case of the GEM-4 n_c scales linearly with the density and does not depend on the temperature. For the PSM we found numerical data, which indicates a linear dependence on both the density ρ^* and the temperature T^* (see Figures 24 and 25).

Similar as the lattice constant, also the parameter α is a unique function of the ratio ρ^*/T^*, as predicted (see Figures 26 and 27).

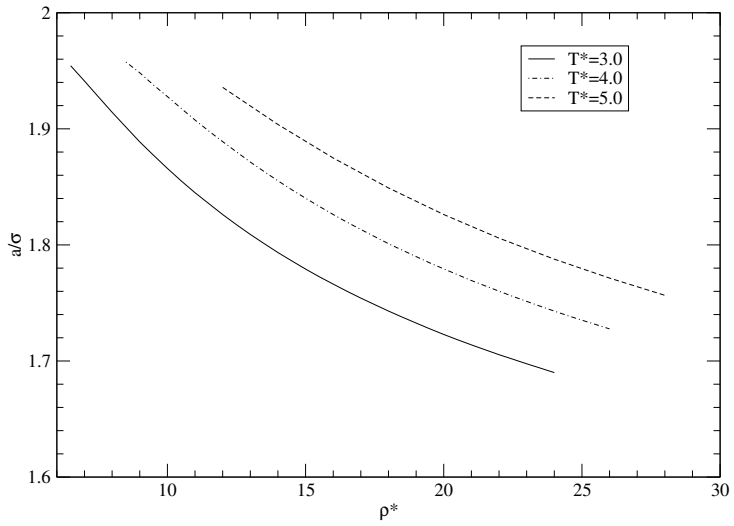

Figure 22: The lattice constant a/σ as a function of the reduced number density ρ^* as obtained from DFT for different temperatures T^*.

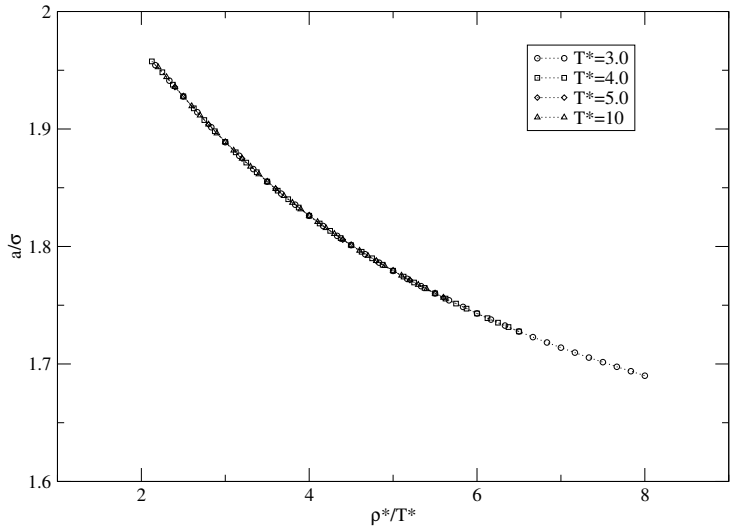

Figure 23: The lattice constant a/σ as a function of the ratio between the reduced density and the reduced temperature ρ^*/T^* as obtained from DFT. All data results obtained for different temperatures T^* coincide on one single curve.

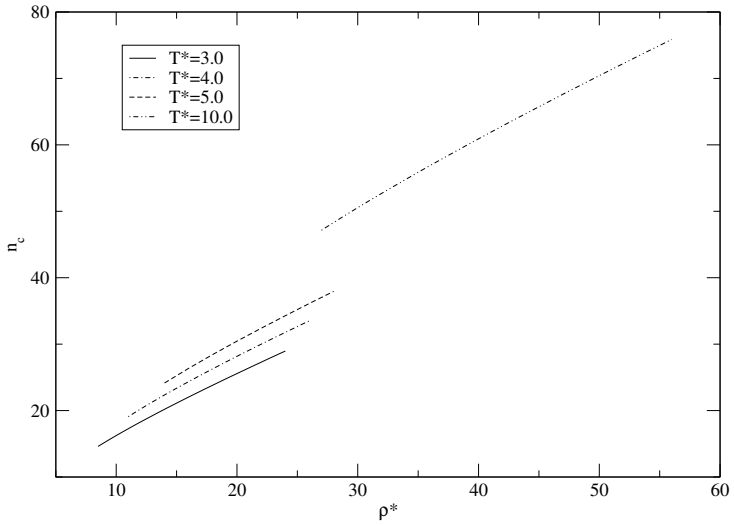

Figure 24: The cluster site occuppancy n_c as a function of the reduced number density ρ^* as obtained by DFT for different temperatures T^*.

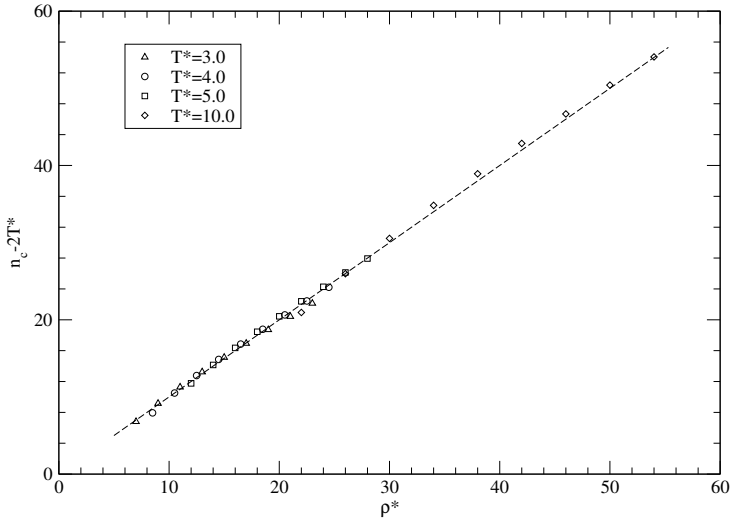

Figure 25: The cluster site occupancy n_c shifted down by $2T^*$ as a function of the reduced number density ρ as obtained by DFT for different temperatures. All data points from different temperatures T^* conincide with good accordance on the same straight line, indicating a linear dependence of the site occupancy on the density ρ and the temperature T^*. Linear regression leads to the relation $n_c = 2T^* + \rho^*$ for the site occuppancy.

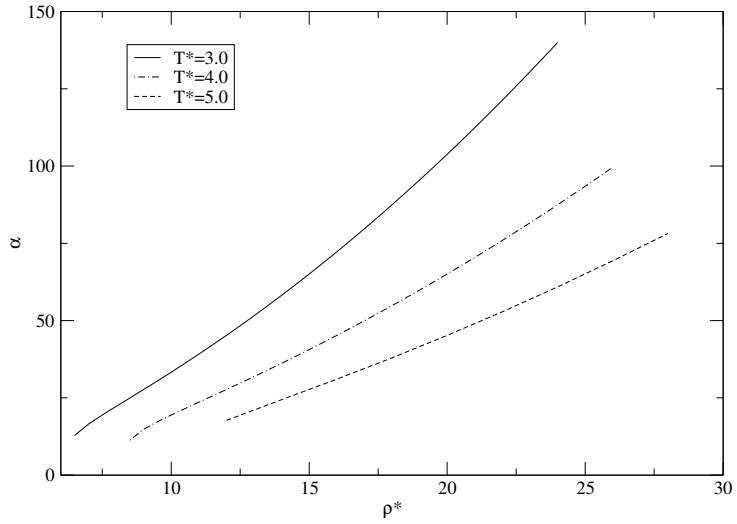

Figure 26: The parameter α as a function of the reduced number density ρ^* at different temperatures T^*.

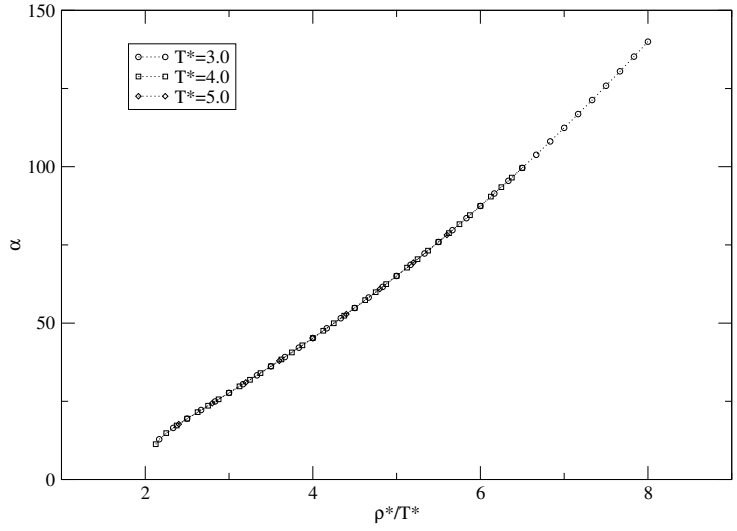

Figure 27: The parameter α as a function of the ratio between the reduced number density and the reduced temperature ρ^*/T^* at different temperatures T^*. All data points coincide on one single curve.

$\{\kappa, \tau\}$	Ω^*
$\{0.3, 0.7\}$	0.9919
$\{0.5, 0.7\}$	0.9625
$\{0.3, 0.5\}$	0.9865
$\{0.5, 0.5\}$	0.9375

Table 1: The field content Ω^* of the four differently dimensioned cores.

4.2 Results for the cmPSM

In this work, we investigated four different sets of parameters κ and τ for the cmPSM:

$$\{\kappa, \tau\} = \{0.5, 0.5\}, \{0.3, 0.5\}, \{0.5, 0.7\}, \{0.3, 0.7\}. \tag{97}$$

As a quantitative measure to characterize the core we introduce the dimensionless field content $\Omega^* \equiv \Omega/\sigma^3$, where Ω is defined by

$$\Omega = 4\pi \int_0^\sigma dr r^2 \Phi(r). \tag{98}$$

Table 1 enlists the field content for the four parameter sets. Obviously, $\Omega^* = 1$ for the PSM.

MSA for the cmPSM

In order to test the validity of the MSA closure for the cmPSM, we compare the pair correlation function $g(r)$ obtained via the MSA closure to the results from MC simulation. We found that the MSA closure gives acceptable results for the cmPSM for all four sets of parameters κ and τ, at temperatures $T^* > 2.0$ (see Figures 28 to 32).

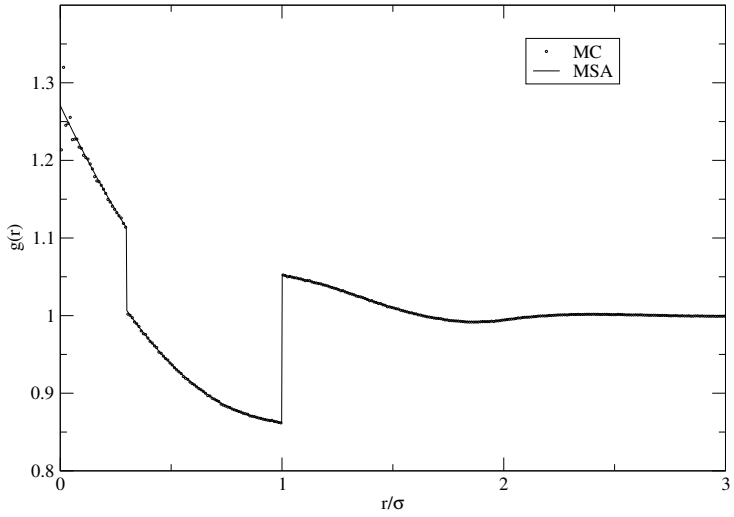

Figure 28: The pair correlation function $g(r)$ for the cmPSM with $\kappa = 0.3$, $\tau = 0.5$ and at temperature $T^* = 5.0$ and density $\rho^* = 4.0$ as obtained via MSA compared to MC simulation results.

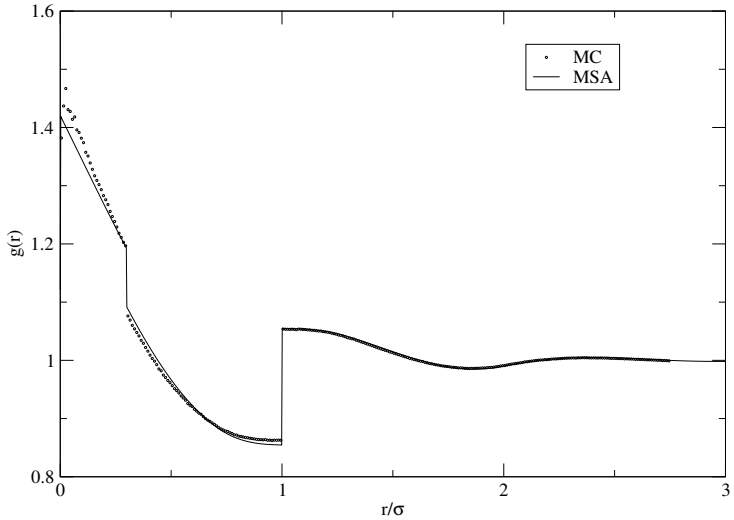

Figure 29: The pair correlation function $g(r)$ for the cmPSM with $\kappa = 0.3$, $\tau = 0.5$ and at termperature $T^* = 5.0$ and density $\rho^* = 6.0$ as obtained via MSA compared to MC simulation results.

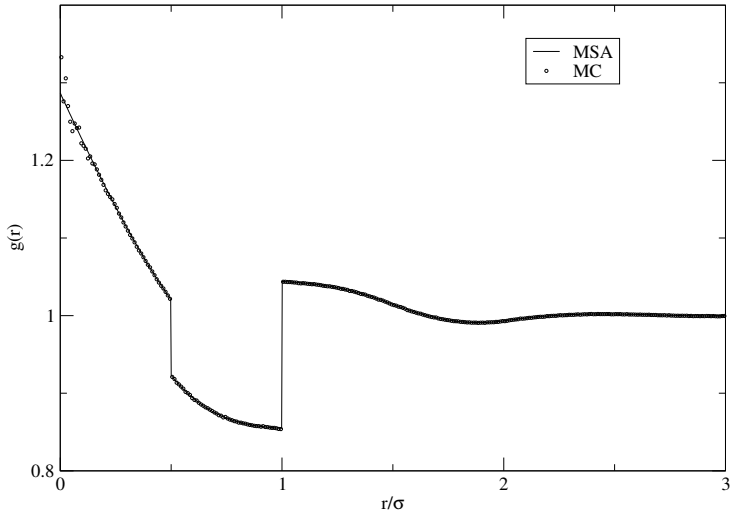

Figure 30: The pair correlation function $g(r)$ for the cmPSM with $\kappa = 0.5$, $\tau = 0.5$ and at termperature $T^* = 5.0$ and density $\rho^* = 6.0$ as obtained via MSA compared to MC simulation results.

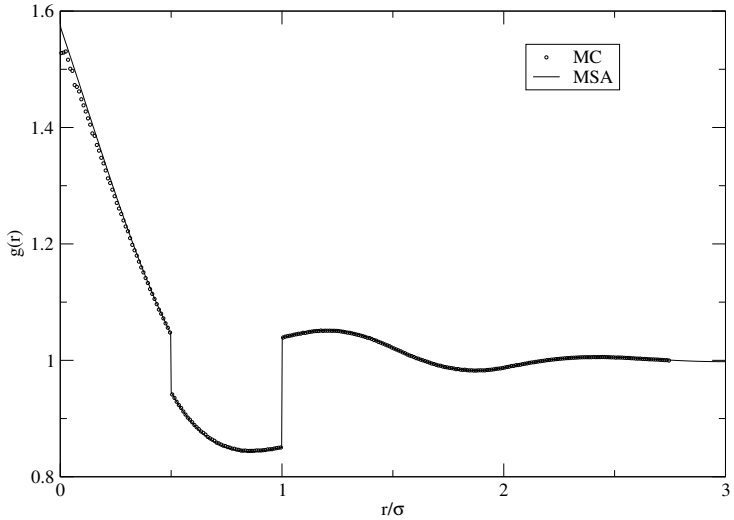

Figure 31: The pair correlation function $g(r)$ for the cmPSM with $\kappa = 0.5$, $\tau = 0.5$ and at termperature $T^* = 5.0$ and density $\rho^* = 6.0$ as obtained via MSA compared to MC simulation results.

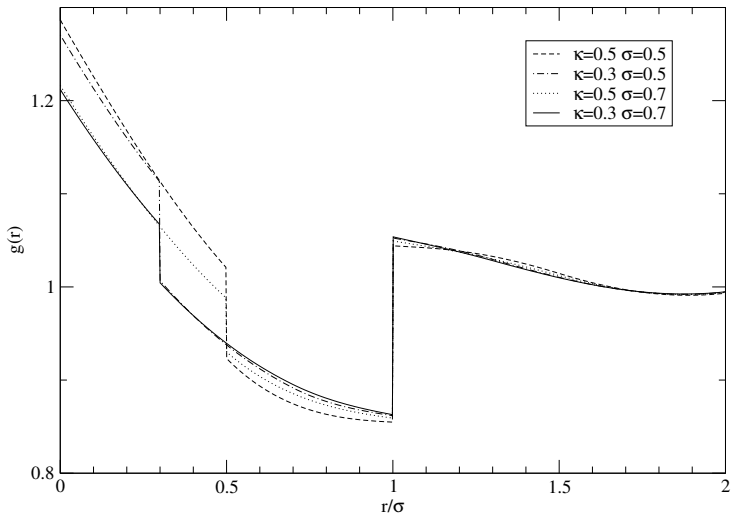

Figure 32: The pair correlation function $g(r)$ for the cmPSM with different values of κ and τ at termperature $T^* = 5.0$ and density $\rho^* = 4.0$ as obtained via MSA.

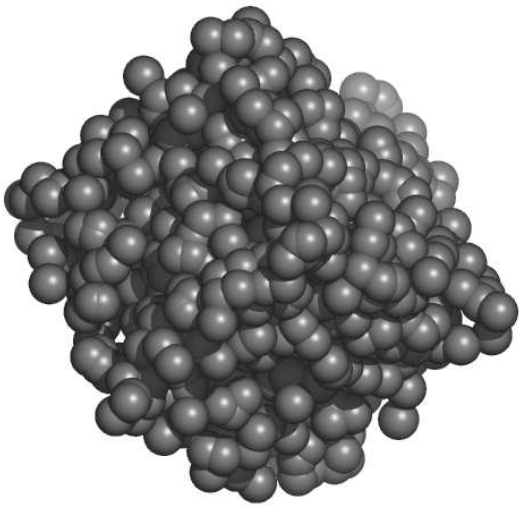

Figure 33: A simulation snapshot of the cmPSM with parameters $\kappa = 0.5$ and $\tau = 0.5$ at temperature $T^* = 5.0$ and density $\rho^* = 4.0$. The particles form clusters, but the system is not yet an ordered phase.

Comparison with simulation

MC simulations have been performed at the points

$$\{\rho^*, T^*\} = \{4,3\}, \{10,3\}, \{12,3\}, \{4,4\}, \{6,4\}, \{4,5\}, \{6,5\}, \{8,5\} \quad (99)$$

for all different parameter sets.

(see Figures 50 to 53).

We found the fcc lattice to be a stable structure for the cmPSM with all different sets of parameters κ and τ (see Figures 34 to 36).

As far as the density profile of the clusters $\rho_{\mathrm{cl}}(r)$ (40) is concerned, the accordance of DFT and MC-simulation is not as good as in the case of the PSM. The one-particle density profiles obtained from MC-simulations slightly deviate from the Gaussian shape . Contrary to our intuitive estimate, that the Gaussian peaks would be more pronounced with respect to the PSM, due to the locally attractive core, the density profile is flattened. The largest deviations occurred for parameters $\kappa = 0.5$ and $\tau = 0.5$, which among all investigated sets represents the strongest core (see Figures 37 to 40).

In order to improve the results, a more sophisticated ansatz for the one-particle density profile would be necessary.

The results provided by DFT for the free energies of the solid phase are of course affected by the ansatz for the one-particle density. In the case of $\kappa = 0.3$ and $\tau = 0.7$, which represents the weakest investigated core, the DFT slightly overestimates the free energies, that were measured in simulations, whereas in all other cases DFT underestimates the free energies (see Figure 41) .

For our purposes, however, the accordance of DFT and simulation was acceptable.

The results obtained from IET for the free energies in the fluid phase are in good agreement with the simulations. For the strongest investigated core ($\kappa = 0.5$ and $\tau = 0.5$) the MSA closure slightly underestimates the free energy (see Figures 42 to 45).

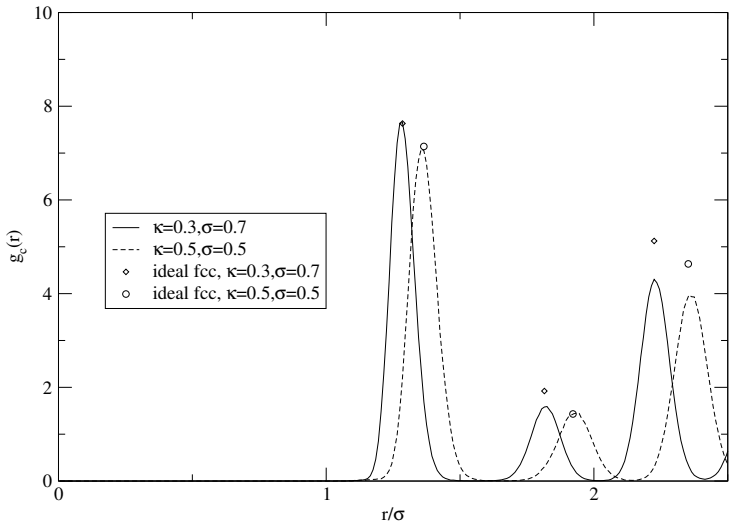

Figure 34: The cluster pair correlation function $g_c(r)$ of the cmPSM for two different sets of parameters κ and τ at temperature $T^* = 3.0$ and density $\rho^* = 12.0$ as obtained by MC simulations. The diamonds and squares denote the positions of the peaks of the pair correlation function of an ideal fcc-lattice at the respective temperature and density.

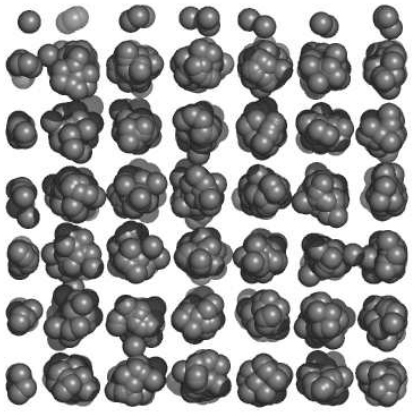

Figure 35: A snapshot of an MC simulation of the cmPSM with $\kappa = 0.5$ and $\tau = 0.5$ at $\rho^* = 12.0$ and $T^* = 3.0$. The size of the particles in the figure is arbitrarily chosen in order to emphasize the lattice structure of the system.

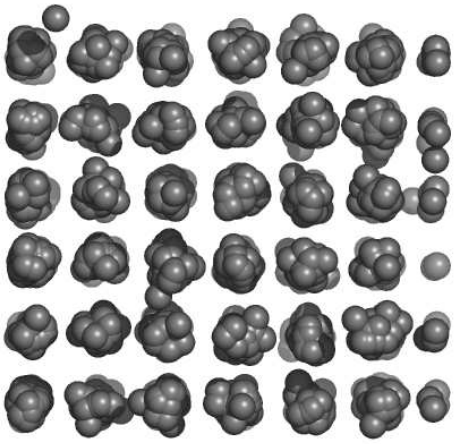

Figure 36: A snapshot of an MC simulation of the cmPSM with $\kappa = 0.5$ and $\tau = 0.5$ at $\rho^* = 12.0$ and $T^* = 3.0$. The size of the particles in the figure is arbitrarily chosen in order to emphasize the lattice structure of the system.

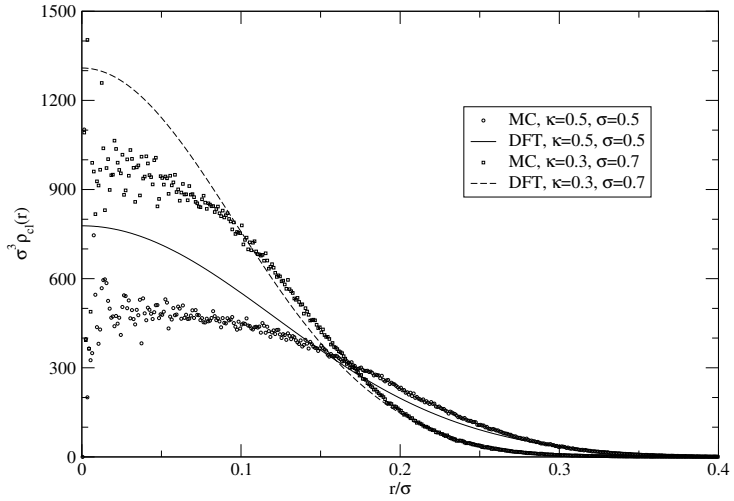

Figure 37: Comparison of the density profile of the clusters $\rho_{\mathrm{cl}}(r)$ in the solid phase for the cmPSM with two different sets of parameters κ and τ as obtained by DFT and MC-simulation at $\rho^* = 12.0$ and $T^* = 3.0$.

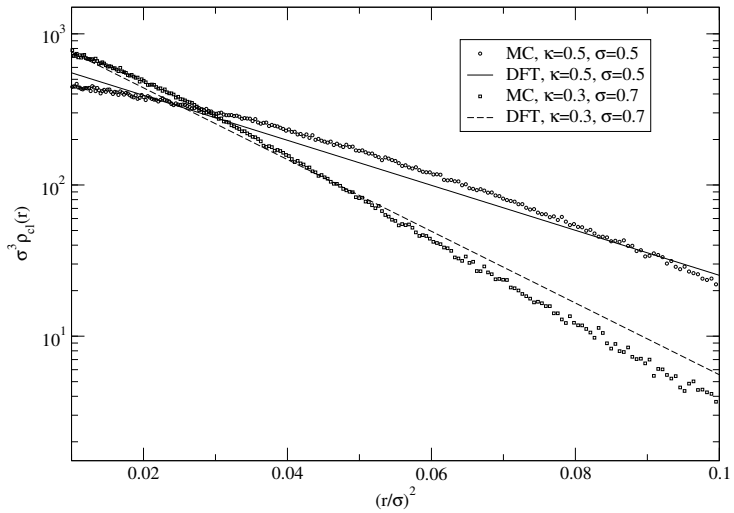

Figure 38: Comparison of the density profile of the clusters $\rho_{\mathrm{cl}}(r)$ in the solid phase as a function of r^2/σ^2 for the cmPSM with two different sets of parameters κ and τ as obtained by DFT and MC simulation at $\rho^* = 12.0$ and $T^* = 3.0$.

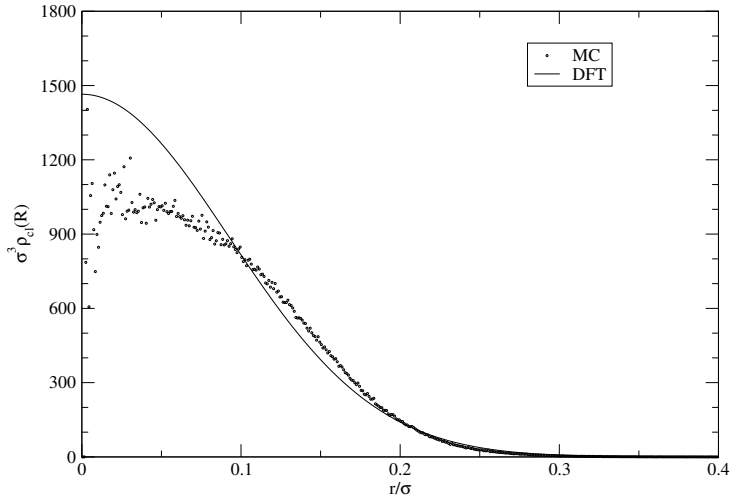

Figure 39: Comparison of the density profile of the clusters in the solid phase for the cmPSM with parameters $\kappa = 0.3$ and $\tau = 0.5$ as obtained by DFT and MC simulation at $\rho^* = 12.0$ and $T^* = 3.0$.

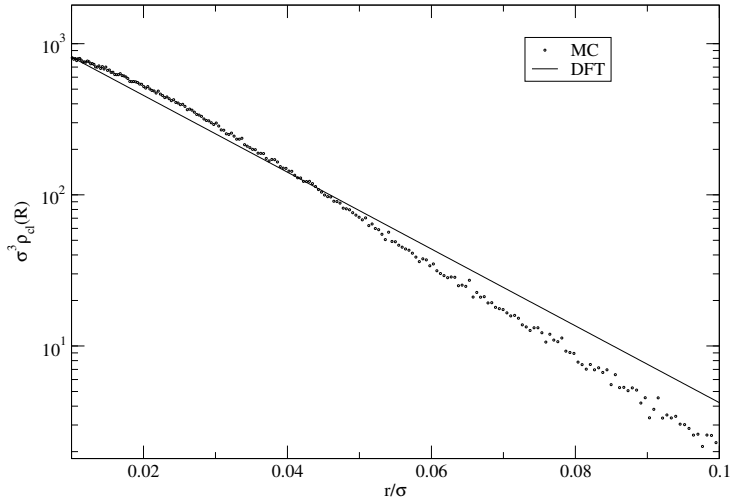

Figure 40: Comparison of the density profile of the clusters $\rho_{\mathrm{cl}}(r)$ in the solid phase as a function of r^2/σ^2 for the cmPSM with parameters $\kappa = 0.3$ and $\tau = 0.5$ as obtained by DFT and MC simulation at $\rho^* = 12.0$ and $T^* = 3.0$.

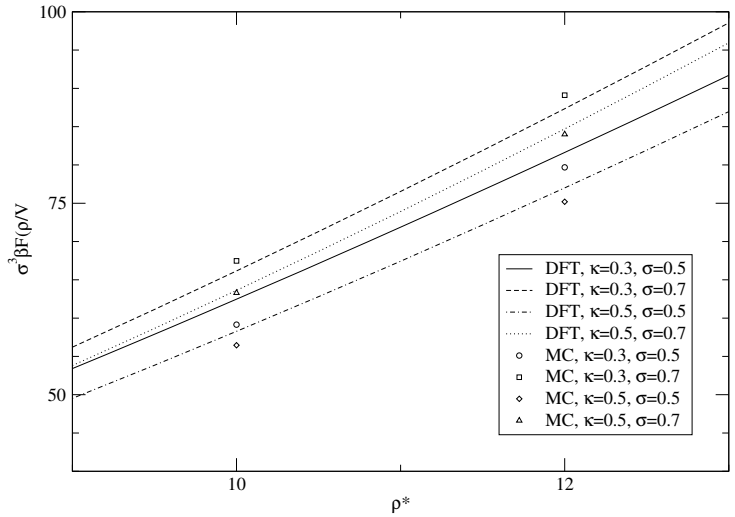

Figure 41: The free energy per volume $\sigma^3 \beta F/V$ as a function of the reduced number density ρ^* for the cmPSM with four different sets of parameters κ and τ at temperature $T^* = 3.0$ as obtained from DFT. The circles denote results from MC simulations .

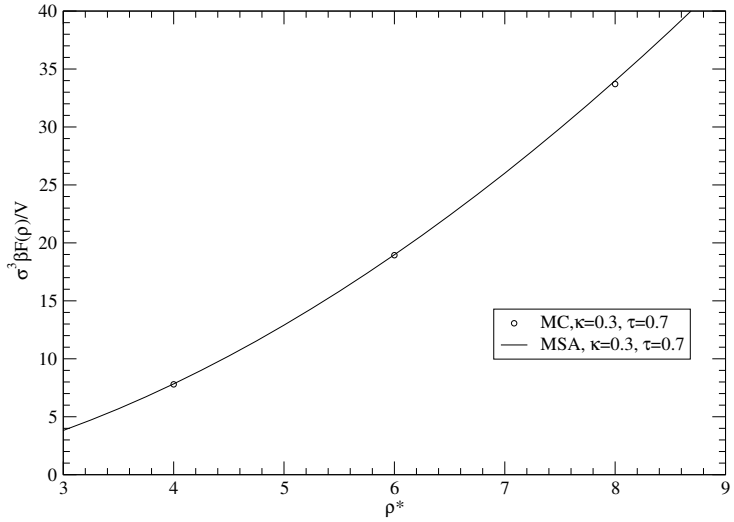

Figure 42: The free energy per volume $\sigma^3\beta F/V$ as a function of the reduced number density ρ^* for the cmPSM with parameters $\kappa = 0.3$ and $\tau = 0.7$ at temperature $T^* = 5.0$ as obtained from IET. The circles denote results from MC simulations .

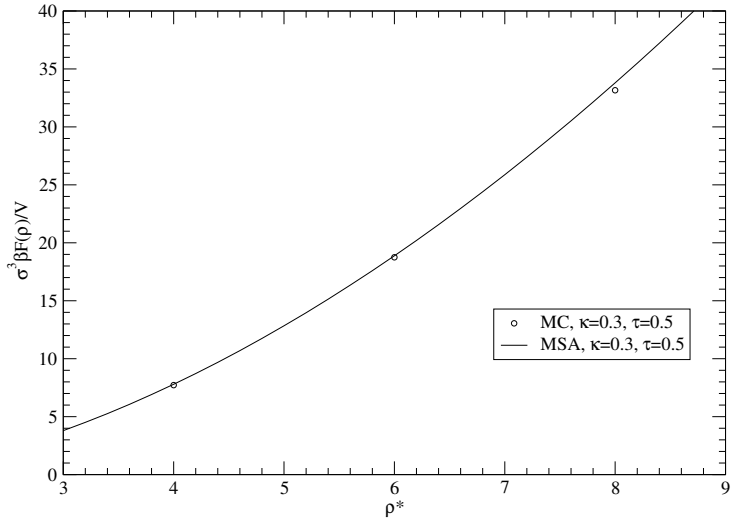

Figure 43: The free energy per volume $\sigma^3\beta F/V$ as a function of the reduced number density ρ^* for the cmPSM with parameters $\kappa = 0.3$ and $\tau = 0.5$ at temperature $T^* = 5.0$ as obtained from IET. The circles denote results from MC simulations .

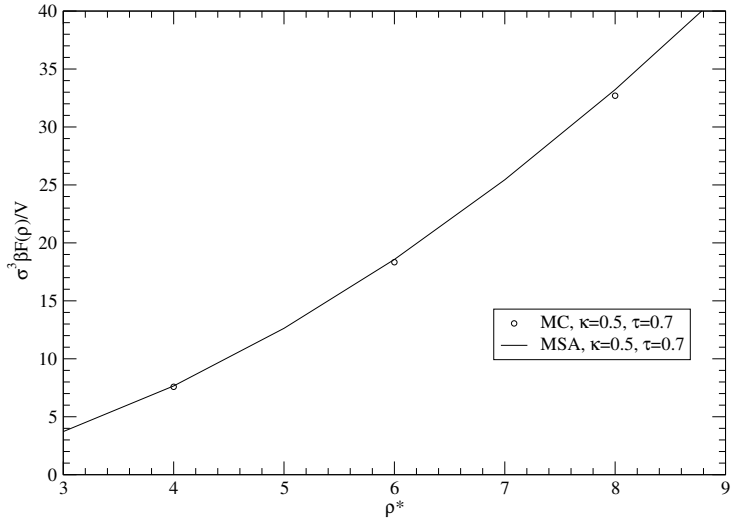

Figure 44: The free energy per volume $\sigma^3\beta F/V$ as a function of the reduced number density ρ^* for the cmPSM with parameters $\kappa = 0.5$ and $\tau = 0.7$ at temperature $T^* = 5.0$ as obtained from IET. The circles denote results from monte-carlo simulations .

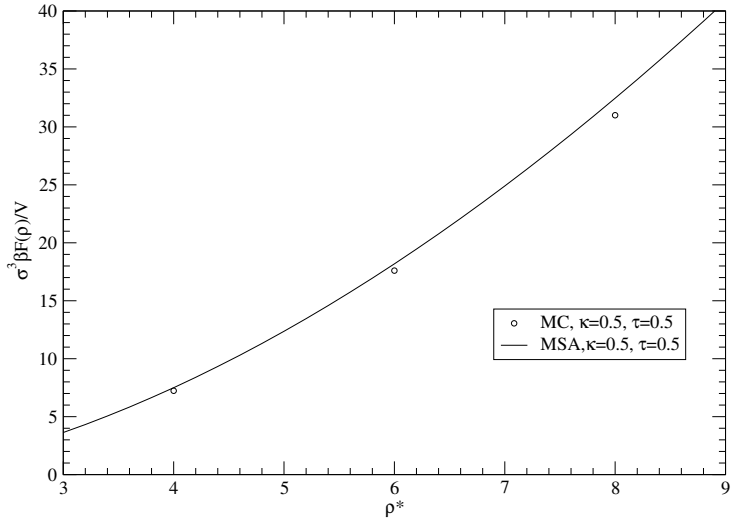

Figure 45: The free energy per volume as a function of the reduced number density ρ^* for the cmPSM with parameters $\kappa = 0.5$ and $\tau = 0.5$ at temperature $T^* = 5.0$ as obtained from IET. The circles denote results from MC simulations .

The phase diagrams

In order to work out the phase diagram of the cmPSM a common tangent construction was performed for temperatures ranging from $T^* = 2.0$ to $T^* = 6.0$. The MSA closure in the framework of IET was used to calculate the free energies in the liquid phase while DFT was used to calculate the free energies of the solid phase.

The coexistence region was found be wedge-shaped, similar as in the case of the PSM and the GEM-4. Contrary to these two models, for the cmPSM the boundaries of the coexistence region slightly deviate from straight lines. The largest deviations are found for parameters $\kappa = 0.5$ and $\tau = 0.5$, which represent the strongest invstigated core (see Figures 46 to 49). Figures 50 to 53 display the points $\{\rho^*, T^*\}$ where MC simulations have been performed.

Due to the locally attractive core region in the cmPSM, we expected the freezing lines to be steeper than in the PSM, which in fact turned out to be true. The slopes of the freezing lines and the melting lines are shown in Figures 54 and 55, respectively. Figure 56 shows the region of the first minimum of the Fourier transforms of the potential for the PSM and the cmPSM. A comparison of the numerical values of the first minimum $|\tilde{\Phi}(Q^\star)|$ reveals, that these values qualitatively correspond to the respective slopes of the freezing lines, e.g., the cmPSM with $\kappa = 0.5$ and $\tau = 0.5$ has the lowest minimum and the highest slope, the cmPSM with $\kappa = 0.5$ and $\tau = 0.7$ has the second lowest minimum and the second highest slope and so on. Hence the theoretical prediction from IET (see section 3.2.1) is met. Note, that for the investigated temperatures the cmPSM with $\kappa = 0.3$ and $\tau = 0.5$ freezes at lower densities than the cmPSM with $\kappa = 0.5$ and $\tau = 0.7$. The slope of the freezing line, however, is larger in the latter case.

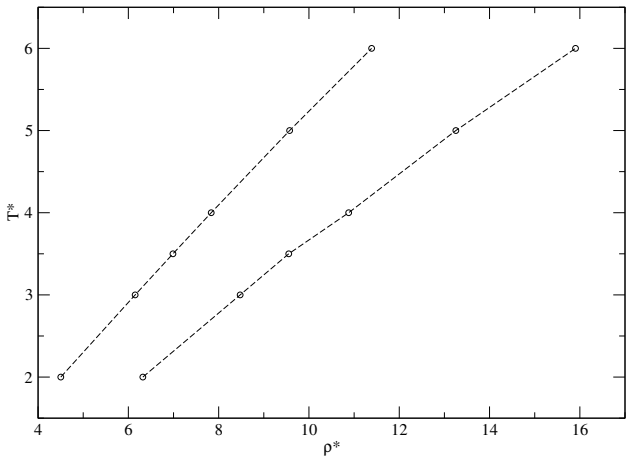

Figure 46: The phase diagram of the cmPSM with $\kappa = 0.3$ and $\tau = 0.7$ in the (T^*, ρ^*)-plane. The lines confine the region where liquid and the solid phases coexist. The circles denote the data points, that were obtained from common tangent construction.

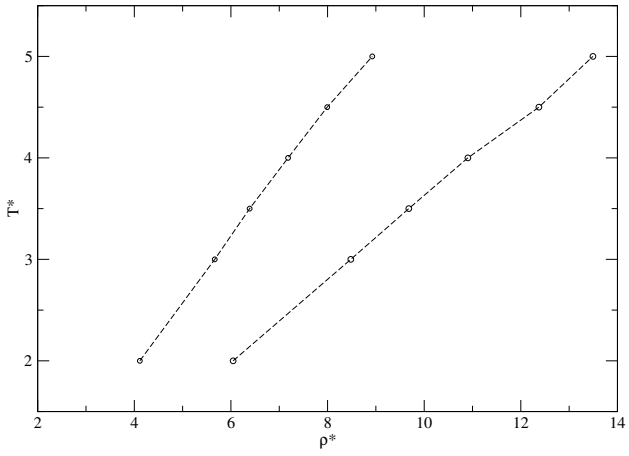

Figure 47: The phase diagram of the cmPSM with $\kappa = 0.3$ and $\tau = 0.5$ in the (T^*, ρ^*)-plane. The lines confine the region where liquid and the solid phases coexist. The circles denote the data points, that were obtained from common tangent construction.

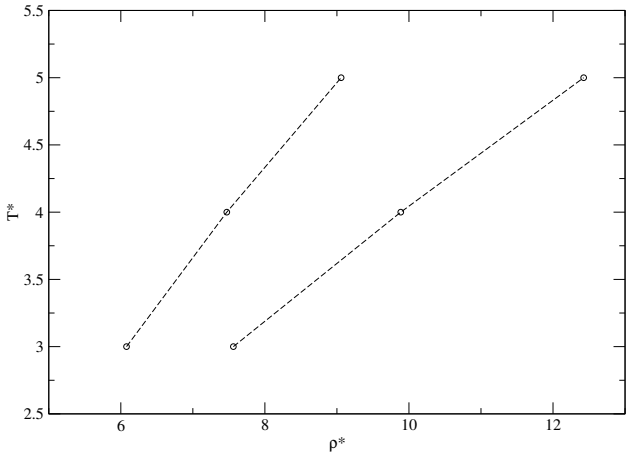

Figure 48: The phase diagram of the cmPSM with $\kappa = 0.5$ and $\tau = 0.7$ in the (T^*, ρ^*)-plane. The lines confine the region where liquid and the solid phases coexist. The circles denote the data points, that were obtained from common tangent construction.

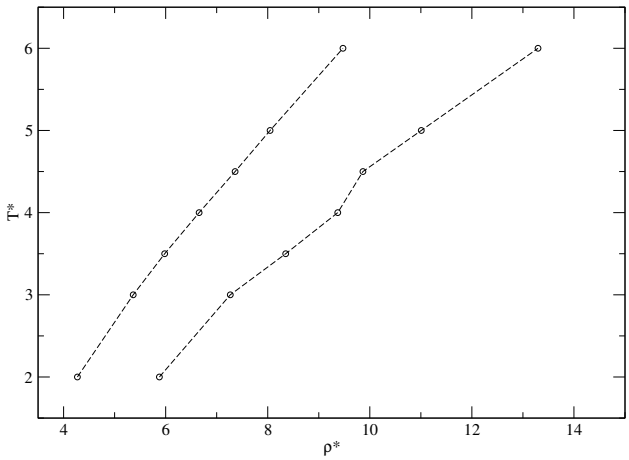

Figure 49: The phase diagram of the cmPSM with $\kappa = 0.5$ and $\tau = 0.5$ in the (T^*, ρ^*)-plane. The lines confine the region where liquid and the solid phases coexist. The circles denote the data points, that were obtained from common tangent construction.

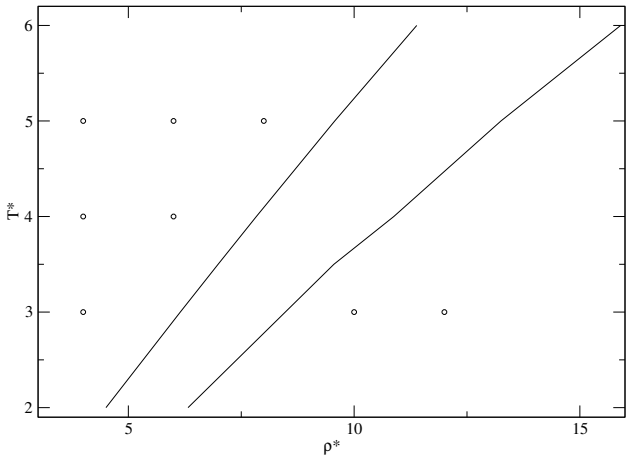

Figure 50: The phase diagram of the cmPSM with $\kappa = 0.3$ and $\tau = 0.7$ in the (T^*, ρ^*)-plane. The lines confine the region where liquid and the solid phases coexist. The circles denote the points $\{T^*, \rho^*\}$, where MC-simulations were performed.

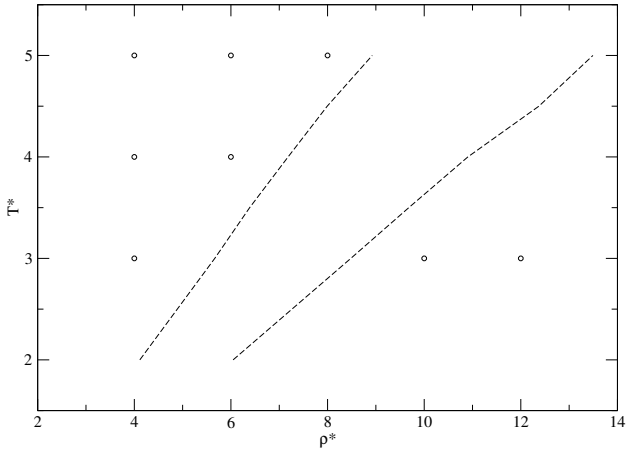

Figure 51: The phase diagram of the cmPSM with $\kappa = 0.3$ and $\tau = 0.5$ in the (T^*, ρ^*)-plane. The lines confine the region where liquid and the solid phases coexist. The circles denote the points $\{T^*, \rho^*\}$, where MC-simulations were performed.

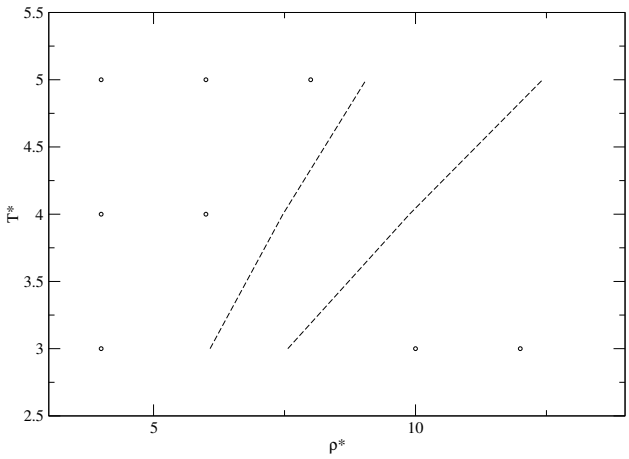

Figure 52: The phase diagram of the cmPSM with $\kappa = 0.5$ and $\tau = 0.7$ in the (T^*, ρ^*)-plane. The lines confine the region where liquid and the solid phases coexist. The circles denote the points $\{T^*, \rho^*\}$, where MC-simulations were performed.

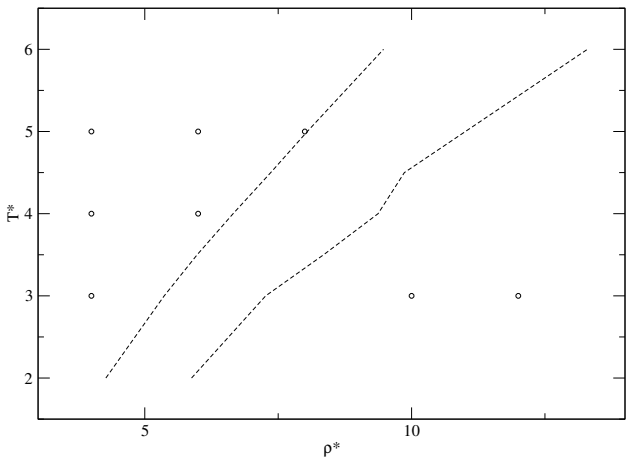

Figure 53: The phase diagram of the cmPSM with $\kappa = 0.5$ and $\tau = 0.5$ in the (T^*, ρ^*)-plane. The lines confine the region where liquid and the solid phases coexist. The circles denote the points $\{T^*, \rho^*\}$, where MC-simulations were performed.

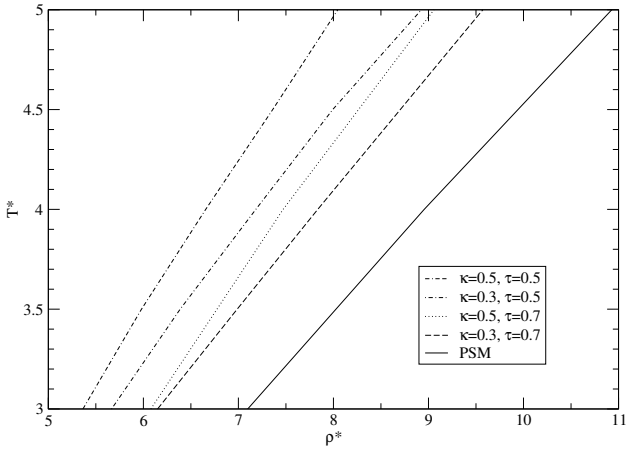

Figure 54: The freezing lines for the cmPSM with different sets of parameters κ and τ compared to the freezing line of the PSM.

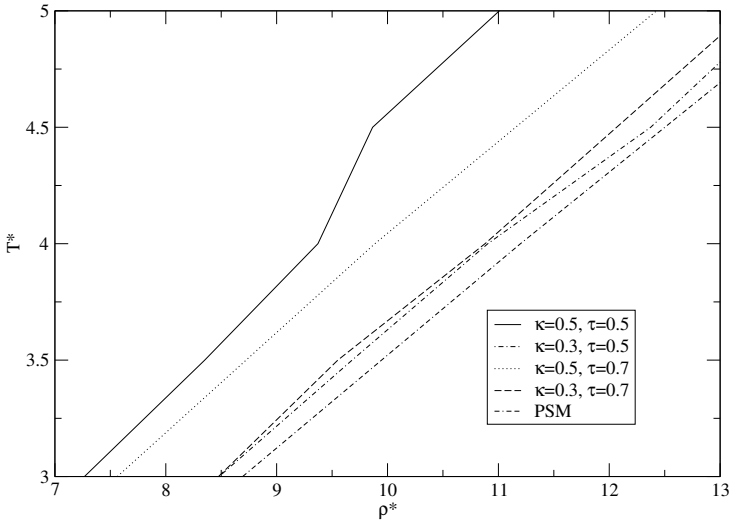

Figure 55: The melting lines for the cmPSM with different sets of parameters κ and τ compared to the melting line of the PSM.

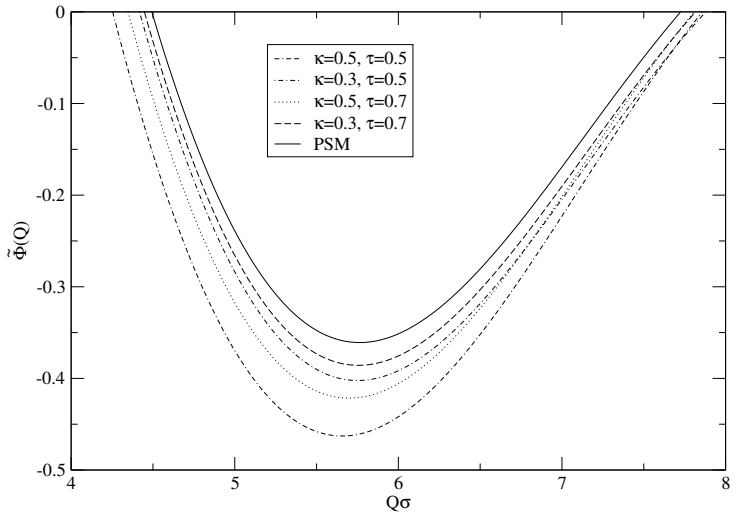

Figure 56: The Fourier transforms of the interaction potential $\tilde{\Phi}(Q)$ in the regio of the first minimum.

The solid phase of the cmPSM

In order to improve clarity, the data curves for the different core modifications are depicted in the same style in all figures throughout this section.

At given temperature and for densities $\rho^* > 13.0$ the lattice constant of the cmPSM was found to be larger than in the case of the PSM. The largest lattice constant is reached for parameters $\kappa = 0.5$ and $\tau = 0.5$, which represents the strongest investigated core modification. According to equation (51) a similar behaviour is observed for the site occupancy n_c. At given temperature and densities $\rho^* > 13.0$ the site occupancy of the cmPSM was found to be larger than in the case of the PSM. Again, for parameters $\kappa = 0.5$ and $\tau = 0.5$, the largest value is reached (see Figures 57 to 59).

We interprete the behaviour as follows: due to the locally attractive core, in the cmPSM the energy cost of adding one particle to a cluster is less than in the PSM. Thus the site occupancy of the cmPSM is higher at a given point in the region of the phase diagram where the solid phase is stable.

Ordering the different parameter sets according to the value of the first minimum of the Fourier tramsorm of the potential $|\tilde{\Phi}(Q^\star)|$ beginning with the smallest, leads to

$$\{\kappa, \tau\} = \{0.3, 0.7\}, \{0.3, 0.5\}, \{0.5, 0.7\}, \{0.5, 0.5\} \tag{100}$$

Note, that the above order of the different core modifications is maintained in the value of both the lattice constant and the site occupancy, which indicates a close relation between these magnitudes and the core parameters κ, τ.

The parameter α that measures the width of the Gaussians of the one-particle density for the cmPSM was found to be lower than in the case of the PSM for temperatures $T^* > 17.0$. For these temperatures again the order of different core modifications mentioned above (100) is established (see Figure 60).

As far as the theoretical predictions (see section 3.3.1) are concerned, we found that the main features of the PSM are maintained also in the cmPSM. The lattice constant and the parameter α are a unique function of the ratio between density and temperature ρ^*/T^*; at equal values of their ratio the lattice constant attains the same value for all temperatures (see Figures 58 and 61). With increasing density the lattice constant decreases, tending towards a lower limit. Hence, the results meet the theoretical predictions from section 3.3.1.

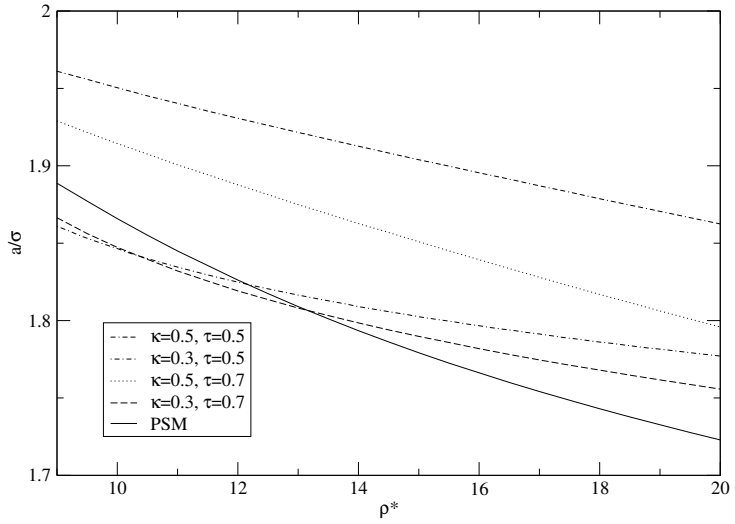

Figure 57: The lattice constant a/σ as a function of the density ρ^* as obtained from DFT at $T^* = 3.0$.

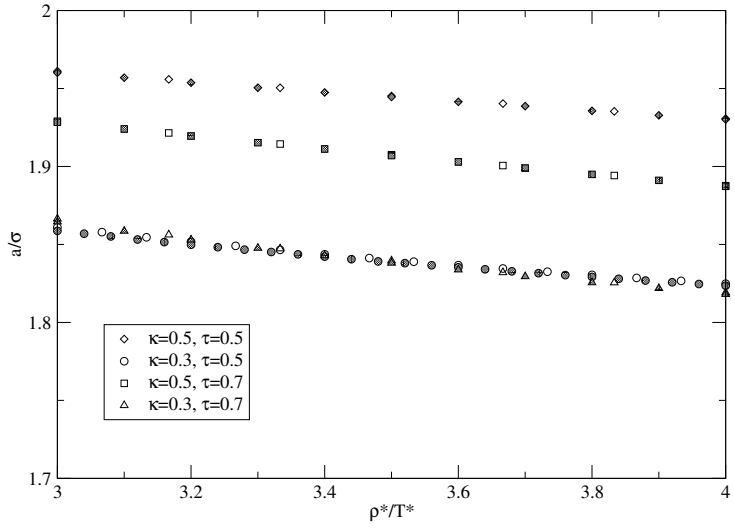

Figure 58: The lattice constant a/σ as a function of the ratio between the density and the temperature ρ^*/T^* as obtained from DFT. For each set of parameters κ and τ the data points are lying on one single curve. The filled symbols correspond to a temperature $T^* = 5.0$ and the empty symbols represent a temperature $T^* = 3.0$.

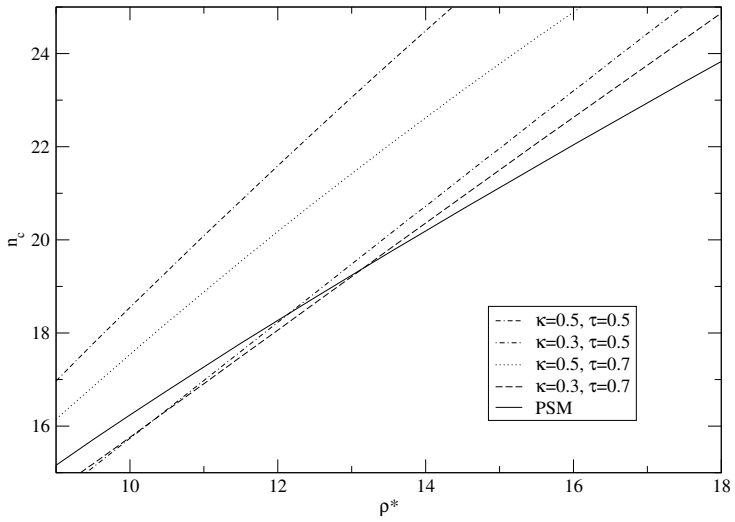

Figure 59: The cluster site occuppancy n_c of the cmPSM as a function of the density ρ^* as obtained by DFT at $T^* = 3.0$.

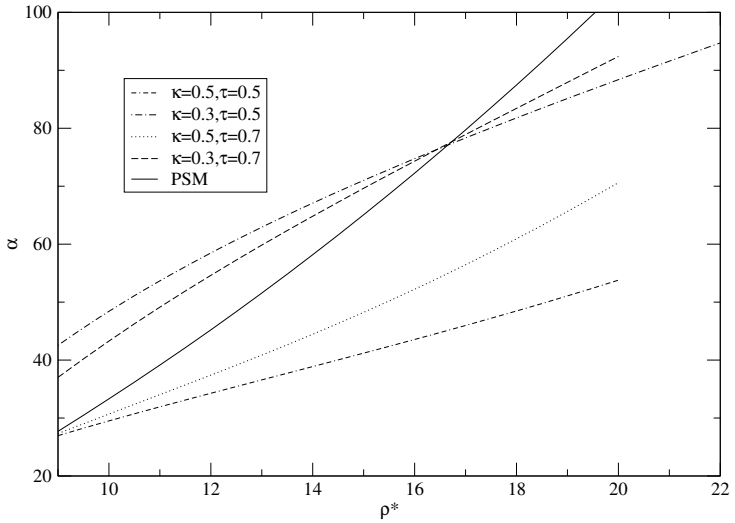

Figure 60: The parameter α as a function of the density ρ^* at $T^* = 3.0$.

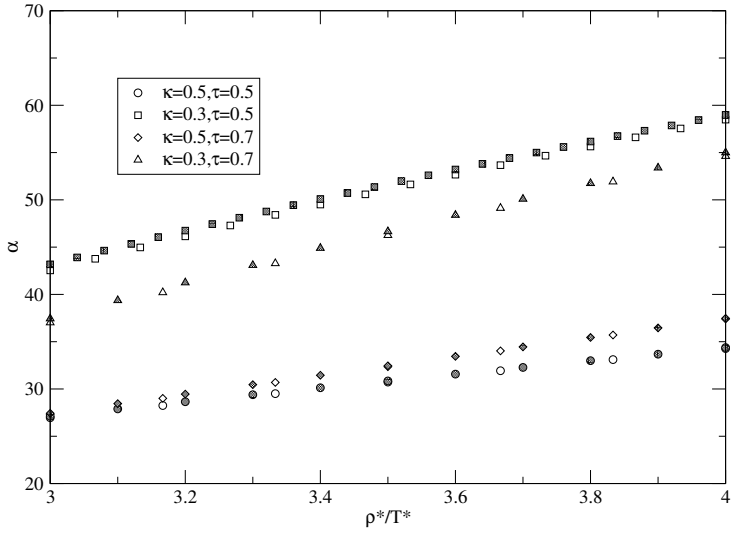

Figure 61: The parameter α as a function of the ratio ρ^*/T^* at different temperatures. The filled symbols correspond to a temperature $T^* = 5.0$ and the empty symbols represent a temperature $T^* = 3.0$.

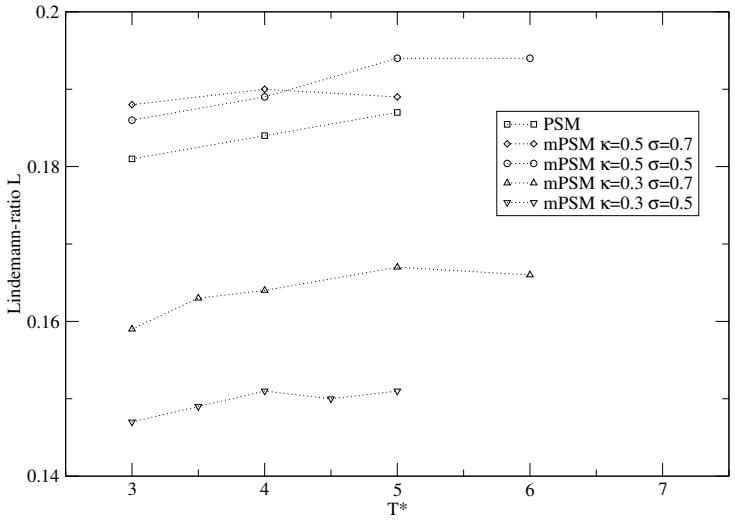

Figure 62: The Lindemann ratio L at freezing for different potential types. The values of the Lindemann ratio at freezing range from 0.16 to 0.195. For a specific type of potential the values of the Lindemann ratio at freezing at different temperatures are close to each other.

5 Summary

In this thesis we studied the phase behaviour of the Penetrable Sphere Model (PSM) and the core modified Penetrable Sphere Model (cmPSM), both being representants of the clustering class of bounded potentials. In the case of the cmPSM we studied four different shapes of the core. In our investigations the free energies for the liquid phase were obtained via the mean spherical approximation (MSA) in the framework of Integral Equation Theory (IET). The free energies of the solid phase were calculated with the help of Density Functional Theory (DFT). We performed numerous Monte-Carlo (MC) simulations in both the liquid and the solid phases in order to check the validity of IET and DFT, respectively, for the investigated models. Throughout the simulation, we measured the free energy of the simulated system using Widom's particle insertion method [13].

As a first result we found that MSA provides excellent results for both the PSM and the cmPSM. The pair correlation functions and the free energies are in good agrreement with the respective simulation results. The data revealed that the format for the density functional in combination with the specific *ansatz* for the one-particle density yields reliable results for the free energies of the solid phase. The fcc lattice was found to be a stable solid structure for all investigated systems. Furthermore we checked the validity of the *ansatz* for the one-particle density by comparison to simulation results. The accordance was found to be good in the case of the PSM, whereas we observed slight deviations from the Gaussian form for the cmPSM. A more sophisticated *ansatz* should be considerd in future investigation. Due to the specific form of the potential a double Gaussian form might be more appropriate.

For all models we quantitatively worked out the phase diagram, calculating the boundaries of the coexistence region between the fluid and the clustered phase by means of common tangent constructions. The slopes of the freezing lines as well as the melting lines qualitatively correspond to the theoretical prediction [4]. Furthermore we compared our results to those obtained by Mladek *et al.* [20] by similar methods for the GEM with index $n = 4$.

As far as the solid phase is concerned, we calculated the equilibrium parameters of the one-particle density profile, i.e., the site occupancy n_c and the width α of the Gaussian clusters and closely inspected their dependence on temperature and density. α and the lattice constant a were found to depend only on the ratio $T^*/\rho*$, the lattice constant attaining a constant limiting

value as the density goes to infinity. Both results qualitatively confirm the theoretical predictions made in recent publications [6][4]. The site occupancy, n_c, linearly depends on the density, the numerical data indicating a relation $n_c = 2T^* + \rho^*$. In our opinion a deeper analysis of the analytic methods proposed by Likos *et al.* [6] would be very useful, in order to fully understand this behaviour from a theoretical point of view.

Finally we calculated the Lindemann ratios at freezing at different temperatures. We found that the ratios attain a model-dependent universal value independent of the temperature.

References

[1] C.N. Likos, Phys. Reports, **348** 267 (2001).

[2] B. M. Mladek, *Exotic phenomena in the phase behaviour of soft matter systems*, PhD Thesis (TU Wien, unpublished), 2002.

[3] F.H. Stilinger, J. Chem: Phys. **65**, 3968 (1976).

[4] C.N. Likos, A. Lang, M. Watzlawek and H. Löwen, Phys. Rev. E **63**, 031206 (2001).

[5] C.N. Likos, M. Watzlawek and H. Löwen, Phys. Rev. E **58** 3135 (1998).

[6] C. N. Likos, B. M. Mladek, D. Gottwald, G. Kahl, J. Chem. Phys. **126**, 224502 (2007).

[7] M. J. Fernaud, E. Lomba and L. L. Lee, J. Chem. Phys. **112**, 810 (2000).

[8] A. Santos, A. Maljewsky, Phys. Rev. E **75**, 021201 (2007).

[9] N. Choudhury, S. K. Ghosh, J. Chem. Phys. **119** 4827 (2003).

[10] C. Marquest, T. A. Witten, J. Phys. (France) **50**, 1267 (1989).

[11] D. Chandler, *Introduction to modern statistical Mechanics* (Oxford University Press, New York, 1987).

[12] J.-P. Hansen and I.R. McDonald, *Theory of Simple Liquids*, (Academic, New York, 1986) 2$^{\text{nd}}$ edition.

[13] D. Frenkel, B. Smit, *Understanding Molecular Simulation*, (Academic Press, San Diego, 1996).

[14] R. Evans in *Fundamentals of inhomogeneous Fluids* edited by D. Henderson (Morcel Dekker, New York ,1992).

[15] L. S. Ornstein, F. Zernike, Proc. Akad. Sci. (Amsterdam) **17**, 793 (1914).

[16] J. K. Percus, G. J. Yevick, Phys. Rev. **110**, 1 (1958).

[17] J. M. J. vann Leeuwen, J. Groenveld and J. De Boer, Physica **25**, 792 (1959).

[18] J. L. Lebowitz and J. Percus, Phys. Rev. **144**, 217 (1966).

[19] J.-P. Hansen and L. Verlet, Phys. Rev. **184**, 151 (1969).

[20] B. Mladek, D.Gottwald, G. Kahl, M. Neumann and C. Likos, Phys. Rev. Letters **96**, 045701 (2006).

[21] A. J. Archer, Phys. Rev. E **72**, 051501 (2005).

[22] D. Gottwald, *Genetic algorithms in condensed matter theory*, PhD Thesis (TU Wien, unpublished), 2005.

[23] N. W. Ashcroft, N. D. Mermin,*Solid State Physics*,(Saunders College, Philadelphia, 1976).

[24] N. G. van Kampen, *Stochastic Processes in Physics and Chemistry* (North-Holland Physics Publishing, Amsterdam, 1981).

[25] N. Metropolis, A. Rosenbluth, M. Rosenbluth, A. Teller and E. Teller, J. Chem. Phys. **21**, 1087 (1953).

[26] B. Widom, J. Chem: Phys., **39**, 2802 (1978).

[27] F. A. Lindemann, Phys. Z. **11**, 609 (1910).